

1 Protein-Metabolite Interactomics Reveals Novel Regulation of 2 Carbohydrate Metabolism

3
4 Kevin G. Hicks¹, Ahmad A. Cluntun¹, Heidi L. Schubert¹, Sean R. Hackett², Jordan A. Berg¹, Paul G.
5 Leonard^{3,4}, Mariana A. Ajalla Aleixo^{5,‡}, Aubrie Blevins^{1,‡}, Paige Barta¹, Samantha Tilley¹, Sarah Fogarty^{1,21},
6 Jacob M. Winter¹, Hee-Chul Ahn^{6,*}, Karen N. Allen^{7,*}, Samuel Block^{8,*}, Iara A. Cardoso⁵, Jianping Ding^{9,*},
7 Ingrid Dreveny^{10,*}, Clarke Gasper^{11,*}, Quinn Ho^{11,*}, Atsushi Matsuura^{6,*}, Michael J. Palladino^{12,*}, Sabin
8 Prajapati^{13,14,*}, PengKai Sun^{9,*}, Kai Tittmann^{13,14,*}, Dean R. Tolan^{11,*}, Judith Unterlass^{15,*}, Andrew P.
9 VanDemark^{16,*}, Matthew G. Vander Heiden^{8,17,*}, Bradley A. Webb^{18,*}, Cai-Hong Yun^{19,*}, PengKai Zhap^{19,*},
10 Christopher P. Hill¹, Maria Cristina Nonato⁵, Florian L. Muller²⁰, Daniel E. Gottschling², James E. Cox¹,
11 Jared Rutter^{1,21,†}

12
13 ¹Department of Biochemistry, University of Utah School of Medicine, Salt Lake City, UT 84112, USA.

14 ²Calico Life Sciences LLC, South San Francisco, CA 94080, USA.

15 ³Core for Biomolecular Structure and Function, University of Texas MD Anderson Cancer Center, Houston,
16 TX 77054, USA.

17 ⁴Institute for Applied Cancer Sciences, University of Texas MD Anderson Cancer Center, Houston, TX
18 77054, USA.

19 ⁵Laboratório de Cristalografia de Proteínas, Faculdade de Ciências Farmacêuticas de Ribeirão Preto,
20 Universidade de São Paulo, Ribeirão Preto, SP 14040-903, Brazil.

21 ⁶Integrated Research Institute for Drug Development, College of Pharmacy, Dongguk University-Seoul,
22 Goyang, Gyeonggi 10326, The Republic of Korea.

23 ⁷Department of Chemistry, Boston University, Boston, MA 02215, USA.

24 ⁸The Koch Institute for Integrative Cancer Research and Department of Biology, Massachusetts Institute of
25 Technology, Cambridge, MA 02139, USA.

26 ⁹State Key Laboratory of Molecular Biology, Shanghai Institute of Biochemistry and Cell Biology, Center for
27 Excellence in Molecular Cell Science, University of Chinese Academy of Sciences, Shanghai, 200031,
28 China.

29 ¹⁰Biodiscovery Institute, School of Pharmacy, University of Nottingham, Nottingham, NG7 2RD, UK.

30 ¹¹Department of Biology, Boston University, Boston, MA 02215, USA.

31 ¹²Department of Pharmacology & Chemical Biology, University of Pittsburgh, Pittsburgh, PA 15261, USA.

32 ¹³Department of Molecular Enzymology, Göttingen Center of Molecular Biosciences, University of
33 Göttingen, Göttingen 37077, Germany.

34 ¹⁴Department of Structural Dynamics, Max Planck Institute for Biophysical Chemistry, Göttingen 37077,
35 Germany.

36 ¹⁵Department of Oncology and Pathology, Karolinska Institute, Stockholm 171 76, Sweden.

37 ¹⁶Department of Biological Sciences, University of Pittsburgh, Pittsburgh, PA 15260, USA.

38 ¹⁷Dana-Farber Cancer Institute, Boston, MA 02115 USA

39 ¹⁸Department of Biochemistry, West Virginia University, Morgantown, WV 26506, USA.

40 ¹⁹Department of Biophysics, School of Basic Medical Sciences, School of Basic Medical Sciences, Peking
41 University Health Science Center, Beijing 100191, China.

42 ²⁰Department of Cancer Systems Imaging, University of Texas MD Anderson Cancer Center, Houston, TX
43 77054, USA.

44 ²¹Howard Hughes Medical Institute, University of Utah School of Medicine, Salt Lake City, Utah 84112,
45 USA.

46 *These authors are listed alphabetically.

47

48 ‡Current addresses: Department of Molecular Biology, UT Southwestern Medical Center, Dallas, TX
49 75390, USA (AB); Brazilian Nanotechnology National Laboratory, Brazilian Center for Research in Energy
50 and Materials, Campinas, SP 13083-970, Brazil (MAAA).

51

52 †Corresponding author email: rutter@biochem.utah.edu

53

54

55

56

57

58

59 **Abstract**

60 Metabolism is highly interconnected and also has profound effects on other cellular processes. However,
61 the interactions between metabolites and proteins that mediate this connectivity are frequently low affinity
62 and difficult to discover, hampering our understanding of this important area of cellular biochemistry.

63 Therefore, we developed the MIDAS platform, which can identify protein-metabolite interactions with
64 great sensitivity. We analyzed 33 enzymes from central carbon metabolism and identified 830 protein-
65 metabolite interactions that were mostly novel, but also included known regulators, substrates, products
66 and their analogs. We validated previously unknown interactions, including two atomic-resolution

67 structures of novel protein-metabolite complexes. We also found that both ATP and long-chain fatty acyl-
68 CoAs inhibit lactate dehydrogenase A (LDHA), but not LDHB, at physiological concentrations *in vitro*.

69 Treating cells with long-chain fatty acids caused a loss of pyruvate/lactate interconversion, but only in
70 cells reliant on LDHA. We propose that these regulatory mechanisms are part of the metabolic

71 connectivity that enables survival in an ever-changing nutrient environment, and that MIDAS enables a
72 broader and deeper understanding of that network.

73

74 Main Text

75 Metabolites are the small molecule substrates, intermediates, and end products of metabolic
76 pathways, and their physical interactions with proteins are among the most common and important
77 interactions in biology (Fig. 1A). Metabolites are not only the chemical ingredients of metabolic reactions,
78 but also enact enzyme regulation within and between metabolic pathways. Such regulatory interactions
79 enable the maintenance of metabolic homeostasis in an environment where the availability and identity of
80 nutrients are constantly changing. Despite their central importance, progress towards comprehensive
81 identification of protein-metabolite interactions (PMIs) has been limited and sporadic. Unlike interactions
82 involving other biological molecules, where we have robust and generalizable approaches such as co-
83 immunoprecipitation for identifying protein-protein interactions (1) and chromatin immunoprecipitation for
84 elucidating protein-DNA interactions (2, 3), widely applicable strategies to detect PMIs are lacking. Although
85 some progress has been made recently (4), the very nature of many of these biologically important
86 interactions presents a major hurdle to their identification. For example, to maximize the regulatory potential
87 of protein binding, metabolites frequently interact with proteins with an affinity that is sufficiently weak to
88 approximate their dynamic cellular concentrations—often high micromolar to low millimolar. Therefore, we
89 developed the highly sensitive MIDAS (Mass spectrometry Integrated with equilibrium Dialysis for the
90 discovery of Allostery Systematically) platform to enable the systematic discovery of PMIs, including those
91 low-affinity interactions that mediate cellular metabolic homeostasis.

92 The MIDAS platform is built on the biophysical principle of equilibrium dialysis (5) (Fig. 1B). A
93 purified protein is separated from a defined library of metabolites by a semi-permeable dialysis membrane
94 that allows passage of the metabolites but not the protein. After incubation, the system achieves relative
95 equilibrium, such that the concentration of free (i.e. non-interacting) metabolites becomes similar on both
96 sides of the membrane. However, the total concentration of those metabolites that interact with the protein
97 is specifically elevated in the protein-containing chamber (Fig. 1B-purple triangles). The protein is then
98 removed by precipitation and the relative metabolite abundance is quantified by high-throughput flow
99 injection analysis mass spectrometry (FIA-MS). Interestingly, there are also metabolites that are selectively
100 depleted from the protein-containing chamber (Fig. 1B-yellow stars), which likely results from enzymatic
101 conversion or from very high affinity interactions including covalent protein modifications.

102 The MIDAS metabolite library comprises 401 compounds that together represent a sizable fraction
103 of the water-soluble, stable, FIA-MS-detectable, and commercially available human metabolome (Fig. S1A
104 and Data S1). Due to intrinsic differences in chemical structure and ionization properties, not all metabolites
105 could be analyzed using the same FIA-MS parameters. We profiled each metabolite individually for its
106 optimal FIA-MS polarity and mobile phase pH ionization and detection conditions (Data S2), and, guided
107 by these criteria, we divided the library into four pools for multiplexed analysis (Fig. S1B and Data S1).
108 Next, we developed FIA-MS methods, optimized for each pool, that enabled rapid and robust quantitation
109 of the constituent metabolites. Splitting metabolites into pools also allowed us to separate some isomers
110 so that they could be independently quantified, solving a technical shortcoming of FIA-MS.

111 Having established the MIDAS methodology, we performed a pilot validation study using proteins
112 with well-established metabolite interactions. We analyzed three human proteins that converge to regulate
113 the mTORC1 kinase, an important nexus in growth factor signaling: CASTOR1, which binds arginine (6);
114 Sestrin2, which binds leucine, isoleucine, and methionine with decreasing affinity (7); and Rheb, which is a
115 GTPase that hydrolyses GTP to GDP (8) (Fig. S1C). In each case, the known ligands were the most
116 enriched and statistically significant interactors detected: CASTOR1 enriched arginine (Fig. 1C); Sestrin2
117 enriched the leucine/isoleucine/allo-isoleucine isomer group and methionine (Fig. 1D); and Rheb enriched
118 both its substrate, GTP, and its product, GDP, as well as the structurally similar isomer group of ATP and
119 deoxyGTP (Fig. 1E). Thus, MIDAS effectively identified known PMIs, including regulators as well as enzyme
120 substrates and products.

121 The enzymes of glycolysis and related metabolic pathways are of particular interest for MIDAS
122 analysis due to their importance in almost all human cells and the extent of known metabolite interactions.
123 Therefore, we next used MIDAS to profile 33 human enzymes of central carbon metabolism, including
124 enzymes of glycolysis, gluconeogenesis, the tricarboxylic acid (TCA) cycle, and the serine biosynthetic
125 pathway that emerges from glycolysis (Fig. S1C). In total, we identified 830 putative PMIs, the vast majority
126 of which were previously unknown (Table S3). Unsupervised hierarchical clustering (Fig. 2A) and
127 multidimensional scaling (Fig. 2E) of the entire PMI dataset demonstrated that structurally and functionally
128 related proteins frequently have very similar metabolite interactions. For example, phosphoglycerate
129 mutase (PGAM1/2), enolase (ENO1/2), fructose biphosphatase (FBP1/2), and lactate dehydrogenase
130 (LDHA/B) isoforms all clustered closely together. However, this was not observed across all enzyme
131 isoforms nor would it be expected given the known role of enzyme isoforms to enable distinct biological
132 regulation of pathways in different contexts. The PK-M1 isoform of pyruvate kinase was noticeably different
133 from the PK-LR and PK-M2 isoforms, and the IDH2 and IDH3 isoforms of isocitrate dehydrogenase, which
134 catalyze similar chemistry but are evolutionarily and structurally unrelated (9), exhibited distinct metabolite
135 interactomes. Additionally, we observed clustering of multiple NAD(H)-dependent dehydrogenases:
136 glyceraldehyde-3-phosphate dehydrogenase (GAPDH), LDHA, LDHB, mitochondrial malate
137 dehydrogenase (MDH2), and 3-phosphoglycerate dehydrogenase (PHGDH). An analogous clustering of
138 structurally and functionally related metabolites was also apparent, including nicotinamide-containing
139 metabolites and flavin-adenine dinucleotide (Fig. 2B), phosphate-containing organic acids (Fig. 2C), and
140 several nucleotide monophosphates (Fig. 2D).

141 Analysis of the 830 putative PMIs identified by the MIDAS platform showed that carbohydrates
142 were the predominant class of protein-interacting metabolite across central carbon metabolism (Fig. 2F).
143 This likely reflects both substrate/product relationships as well as the allosteric regulation of these enzymes,
144 which are largely involved in carbohydrate metabolism, by upstream or downstream metabolites (i.e.,
145 feedforward and feedback regulation). The majority of non-carbohydrate PMIs included amino acids,
146 nucleotides, and fatty acid derivatives. Such PMIs not only represent substrates and products of enzymes
147 in these pathways, but suggest both intra- and inter-pathway regulation of central carbon metabolism (Fig.

148 2G). Notably, we also observed extensive interactions with metabolites outside of these pathways (Fig.
149 2H). Together, these data likely illustrate the integration of local and distal metabolic information on central
150 carbon metabolism, which provides intermediates for most biosynthetic pathways in the cell.

151 We next selected a subset of PMI datasets from individual proteins in central carbon metabolism
152 (see Fig. 2G) for deeper bioinformatic, biochemical and structural analyses. Enolase catalyzes the
153 penultimate step in glycolysis, and the most enriched and most statistically significant interactor for both
154 isoforms (ENO1 and ENO2) was phosphoserine (pSer, Fig. 3A). Intriguingly, pSer is an intermediate in the
155 serine biosynthetic pathway, which diverges from glycolysis just upstream of enolase. pSer is subsequently
156 converted into serine which in turn allosterically activates the M2 isoform of pyruvate kinase (10), the
157 enzyme immediately downstream of enolase in the glycolytic pathway. Differential scanning fluorimetry
158 (DSF), which measures the thermal stability of a target protein, showed that pSer (but not serine,
159 phosphotyrosine, or phosphate) robustly stabilized both ENO1 ($K_{dapp} = 1.38$ mM) and ENO2 ($K_{dapp} = 1.15$
160 mM) (Fig. 3B), similar to their substrate 2PG ($K_{dapp} = 0.298$ mM and 0.289 mM, respectively). X-ray
161 crystallography of the pSer-ENO2 complex found that pSer asymmetrically bound to the ENO2 dimer at
162 one of the two active sites and partially overlapped with the 2PG phosphate binding site (Fig. 3C, D).
163 Furthermore, pSer promoted an “open” active site conformation relative to the substrate bound complex
164 observed as repositioning of loops 4 and 11 and alpha helices 7 and 11 (Fig. 3D). Surprisingly, pSer only
165 weakly inhibited enolase activity as measured *in vitro* (Fig. S2A), raising the intriguing possibility that this
166 binding event might instead modulate other enolase activities such as one of the reported moonlighting
167 functions (11, 12).

168 MIDAS identified 2-amino-3-phosphonopropionic acid (AP-3), a component of phosphonate
169 metabolism (KEGG), as a putative interactor with fumarase, an enzyme in the tricarboxylic acid cycle that
170 catalyzes the reversible hydration of fumarate to malate, which was also a significant hit (Fig. 3E). AP-3
171 induced the thermal stabilization of fumarase ($K_{dapp} = 0.98$ mM) with similar potency to its substrate,
172 fumarate ($K_{dapp} = 3.87$ mM) (Fig. 3F). Kinetic assays demonstrated that AP-3 competitively inhibited
173 fumarase (Fig. S2B), and, consistent with this, the crystal structure of the complex revealed that AP-3 binds
174 in the active site of fumarase similarly to the known inhibitor citrate (Fig. 3G-H) (13). Although the
175 consequences of fumarase modulation by AP-3 *in vivo* are unclear, these findings demonstrate that MIDAS
176 can identify novel and functional protein-metabolite interactions.

177 MIDAS datasets from additional proteins further confirmed the ability of MIDAS to identify known
178 interactions with substrates, products, and regulators: Glucose-6-phosphate isomerase (GPI) with its
179 substrates, glucose-6-phosphate and fructose-6-phosphate (hexose-6-phosphates) (Fig. 3I);
180 phosphofructokinase (PFKP) with its product (F-1,6BP/G-1,6BP) and a putative alternative substrate,
181 sedoheptulose-7-phosphate, (14) which is an intermediate in the pentose-phosphate pathway (Fig. 3J);
182 glyceraldehyde-3-phosphate dehydrogenase (GAPDH) with its substrate (NAD), and regulators (cyclicAMP,
183 creatine-phosphate, and malonyl-CoA) (15-17) (Fig. 3K); and the M2 isoform of pyruvate kinase (PK-M2)
184 with GDP and multiple amino acid regulators (18) (Fig. 3L). In every case, MIDAS also highlighted intriguing

185 previously unknown interactions with distinct and non-overlapping sets of metabolites. For example, acyl-
186 CoAs, inositol phosphates, nicotinamides, adenine nucleotides, and downstream glycolytic intermediates
187 were found to interact with GPI (Fig. 3I). We also observed interactions between PFKP and several di- and
188 triphosphate nucleotides, thiamine pyrophosphate, as well as with L-5-hydroxytryptophan, an intermediate
189 in the conversion of tryptophan to serotonin (Fig. J). Ins(3,4,5)P₃, 2,3-BPG, and HMG-CoA were identified
190 as novel binding partners for GAPDH (Fig. 3K), while PK-M2 interacted with flavins, a folate, and a thyroid
191 hormone intermediate (Fig. 3L). PK-M2 was previously reported to be allosterically regulated by thyroid
192 hormone T₃, but the significance of this binding is unknown (19).

193 A comparison of MIDAS analyses for multiple isoforms of metabolic enzymes demonstrated both
194 shared and unique metabolite interactions. Fructose biphosphatase (FBP) catalyzes the conversion of
195 fructose-1,6-bisphosphate to fructose-6-phosphate, a rate-limiting step in gluconeogenesis. Both isoforms
196 (FBP1 and FBP2) interact with the known inhibitor AMP in addition to other nucleotide monophosphates.
197 However, only FBP1 showed an interaction with glucosamine-6-phosphate, the rate-limiting intermediate
198 in the hexosamine pathway, which emerges from fructose-6-phosphate (Fig. 3M). Similarly, isoforms of
199 phosphoglycerate mutase (PGAM1 and PGAM2) interacted with a large set of metabolites, almost all of
200 which were identical between them, with the exception of the soluble inositol phosphate inositol-1,3,4-P₃
201 (PGAM1) and PIP₂ and PIP₃ (PGAM2) (Fig. 3N). This might reflect differential membrane recruitment
202 and/or regulation of PGAM isoforms by phosphoinositide kinases, which are activated by growth factor
203 signaling. These PMI data illustrate the power of MIDAS to enable the generation of hypotheses about
204 potential novel regulatory events.

205 Lactate dehydrogenase (LDH) reversibly catalyzes the reduction of pyruvate to lactate coincident
206 with the oxidation of NADH to NAD, a pivotal branchpoint in carbohydrate metabolism. Consumption of
207 pyruvate by LDH competes with the mitochondrial uptake and oxidation by the TCA cycle to maximize ATP
208 production. When mitochondrial pyruvate oxidation is limited, such as in hypoxia or aerobic glycolysis, LDH
209 is critically important to regenerate NAD to enable continued glycolytic flux. Importantly, the LDH reaction
210 is reversible and is also required to utilize lactate, a major circulating carbohydrate in mammals, as a fuel
211 to support cellular functions (20). This firmly places LDH as a key node in carbohydrate metabolism.

212 MIDAS analysis of the two major isoforms of LDH, LDHA and LDHB, revealed interactions with
213 several metabolites, most of which were common to both proteins (Fig. 4A). These included the cofactors
214 NADH and NAD and the structurally related nucleotides nicotinamide mononucleotide (NMN) and FAD, as
215 well as the competitive inhibitor, oxaloacetate (21), and other keto-acids related to the LDH substrates
216 lactate and pyruvate. We also observed two other classes of interacting metabolites, adenosine nucleotides
217 and free and acylated coenzyme A (Fig. 4A, B). To determine if either of these classes represent bona fide
218 PMIs, we first used a thermal shift assay to measure the binding affinity of the three major adenosine
219 nucleotides, AMP, ADP, and ATP, for LDHA and LDHB, and compared to the cofactor NAD (Fig. 4C). ATP
220 interacted with both isoforms with a $K_{dapp} = 0.636$ mM and 0.697 mM, respectively, which is a biologically
221 relevant affinity, given that the generally accepted intracellular steady state ATP concentration is 1–5 mM.

222 The interactions of either LDH isoform with ADP and AMP may not be physiologically relevant given the
223 disparity between the K_d values for each interaction and the cellular concentrations of ADP and AMP (~0.4
224 mM and ~0.04 mM, respectively) (22) (Fig. 4C). Enzymatic activity assays of the two LDH isoforms further
225 supported this conclusion as both AMP and ADP inhibited LDHA and LDHB only at supraphysiological
226 concentrations (Fig. 4D). Interestingly, despite similar binding affinities to both LDHA and LDHB (Fig. 4D),
227 ATP selectively inhibited only the LDHA isoform, with an IC_{50} of 2.3 mM. This discrepancy could potentially
228 relate to the opposing effects of ATP binding on the thermal stability of the two proteins (Fig. 4C). The
229 inhibition of LDHA by ATP appears to be competitive with NAD and lactate (Fig. S3A).

230 Next, we investigated the putative interaction between the LDH isoforms and coenzyme A (CoA)
231 or CoA conjugated to short, medium, or long-chain fatty acids (i.e. acyl-CoAs). Esterification of long-chain
232 (>12 carbons) fatty acids to CoA is required for their intracellular diffusion and transport into the
233 mitochondrial matrix where they undergo β -oxidation to produce ATP. The accumulation of these species
234 has been previously demonstrated to be a signal of carbon fuel excess (23). We observed that acyl-CoAs
235 inhibited LDHA as a function of fatty acid chain length. Neither CoA alone nor any acyl-CoA with a fatty acid
236 chain-length up to eight carbons affected enzyme activity, and C12:0-CoA only weakly inhibited LDHA, with
237 an IC_{50} >100 μ M (Fig. 4E). However, long-chain acyl-CoAs—C16:0-CoA (palmitoyl-CoA), C18:1-CoA
238 (oleoyl-CoA) and C20:0-CoA (arachidoyl-CoA), none of which are in the MIDAS library—were all potent
239 inhibitors of LDHA, with IC_{50} values of ~1 μ M (Fig. 4E). The inhibition of LDHA by palmitoyl-CoA is non-
240 competitive with respect to both NAD and lactate, suggesting that it is binding to LDHA outside of the active
241 site (Fig. S3B). Intriguingly, LDHB, which shares 85% amino acid sequence identity with LDHA, was
242 completely impervious to all tested acyl-CoAs, even at concentrations up to 100 μ M (Fig. 4F).

243 Having observed that palmitoyl-CoA inhibited LDHA, but not LDHB, we employed two orthogonal
244 approaches to test for a physical interaction. Using a thermal stability assay, we found that low micromolar
245 concentrations of palmitoyl-CoA, similar to the IC_{50} , induced the formation of a distinct thermo-labile species
246 of LDHA, while inducing a thermo-stable species of LDHB (Fig. S3C). These data indicate that LDHA and
247 LDHB both directly interact with palmitoyl-CoA with a physiologically relevant low micromolar affinity. Next,
248 we found that purified LDHA and LDHB bound to palmitoyl-CoA immobilized on agarose beads, and that
249 the binding for either protein was disrupted by elution with palmitoyl-CoA but not with buffer or acetyl-CoA
250 (C2:0-CoA) (Fig. S3D).

251 Given that palmitoyl-CoA inhibited LDHA at concentrations within the physiological range, we next
252 tested whether this inhibition is relevant in intact cells. We performed metabolic tracing experiments using
253 H9c2 rat cardiomyoblasts in which we knocked out *Ldha*, *Ldhb*, or both (Fig. S3E). We treated cells with
254 13 C-labeled glucose in the presence or absence of BSA-palmitate, which allows for efficient delivery of the
255 fatty acid into the cell where it can esterified to palmitoyl-CoA (Fig. 4G). We then used mass spectrometry
256 to measure the uptake and assimilation of 13 C into lactate. All four cell lines (WT, *Ldha*^{-/-}, *Ldhb*^{-/-} and *Ldha*^{-/-}
257 *Ldhb*^{-/-}) showed a similar (~80%) increase in intracellular palmitate following incubation with its BSA-
258 conjugate (Fig. S3F). Importantly, palmitate decreased the labelling of lactate from 13 C-glucose, but only in

259 wild-type (WT) and *Ldhb*^{-/-} cells i.e., in cells in which LDHA is still present (Fig. 4H, S3G-H), implying that
260 palmitate inhibition of glucose-to-lactate conversion is completely dependent upon LDHA in this cell line.
261 This result indicates that one or more steps between glucose uptake and LDHA-catalyzed lactate synthesis
262 is inhibited by palmitate treatment. To probe more specifically the uptake and LDH-mediated oxidation of
263 lactate to pyruvate, we performed analogous experiments with ¹³C-lactate (Fig. 4I). Again, we found that
264 treatment with palmitate inhibited the generation of ¹³C-pyruvate in WT and LDHB^{-/-} cells, but pyruvate
265 labeling in *Ldha*^{-/-} or *Ldha*^{-/-} *Ldhb*^{-/-} cells was unaffected (Fig. 4J, S3I-J). These data suggest a novel mode
266 of regulatory crosstalk between fatty acid and carbohydrate metabolism.

267 It is intriguing that we found that both ATP and long-chain acyl-CoAs preferentially inhibit LDHA,
268 but not LDHB. LDHA and LDHB, the two dominant isoforms of lactate dehydrogenase, are expressed in a
269 tissue-specific pattern such that the liver almost exclusively expresses LDHA, while the heart has high
270 expression of LDHB (Fig. S4A, B). Importantly, the IC₅₀ for inhibition by ATP is easily within the range of
271 normal intracellular ATP concentrations, suggesting that LDHA might be partially inhibited in all cells with
272 normal energy status. Given that the liver, the most LDHA-dominant tissue, is capable of catabolizing
273 multiple substrates, inhibition by ATP might be a mechanism to spare carbohydrates for those cell types
274 that are dependent upon them. This is particularly important given the recent demonstration that lactate
275 may be a major carbohydrate fuel consumed by some tissues (20). Likewise, our observation that long-
276 chain acyl-CoAs inhibit LDHA could explain a previously described physiological phenomenon wherein fatty
277 acids, released from the adipose tissue during fasting, inhibit lactate production and increase glucose
278 production in the liver (24). We hypothesize that fatty acyl-CoA-mediated inhibition of LDHA would redirect
279 pyruvate toward gluconeogenesis and away from excretion following its conversion to lactate. Another
280 potential implication of these results lies in the substantial interest in LDHA-specific inhibitors to block
281 aerobic glycolysis in cancers (25, 26). Perhaps the mechanism(s) employed by ATP and acyl-CoAs could
282 be exploited therapeutically.

283 This fatty acid-carbohydrate inter-pathway metabolic regulation is just one potential example of the
284 myriad metabolite-level regulatory events that enforce organismal homeostasis, which is vital to
285 appropriately respond to stressors such as the feed-fast cycle, exercise, and infection. We propose that
286 interactions between proteins and metabolites mediate much of this control. We have validated MIDAS as
287 a robust platform for the discovery of these critical mechanisms, particularly for the detection of very low
288 affinity interactions, which include most of those involving high abundance cellular metabolites. In addition
289 to recent discoveries of functionally important PMIs (27-29), MIDAS now identified hundreds of known and
290 novel putative interactions with the enzymes of central carbon metabolism. Together, these serve as a
291 roadmap for identifying new modes of metabolic regulation as well as previously undescribed alternative
292 substrates. We propose that the comprehensive discovery of such interactions will revolutionize our
293 understanding of cell biology and that MIDAS can empower a renewed focus on this challenging and critical
294 important area of biology.

295

296 **Acknowledgements**

297 We thank members of the Rutter lab for helpful discussions and comments on the manuscript. We thank
298 Roche and Navitor for providing proteins for MIDAS analyses. We thank the University of Utah Mutation
299 Generation and Detection Core for providing CRISPR reagents, cell genotyping services and construction
300 of bacterial expression vectors. We thank the University of Utah Drug Discovery Core Facility for
301 generating the *Ldha* and *Ldhb* mutant cells. Metabolomics analysis was performed in the Metabolomics
302 Core Facility at the University of Utah. Mass spectrometry equipment was obtained through NCRR
303 Shared Instrumentation Grant 1S10OD016232-01, 1S10OD018210-01A1 and 1S10OD021505-01. This
304 work was supported by T32DK091317 and T32DK007115 to KGH, U54DK110858, R35GM131854, and a
305 grant from Calico Life Sciences, LLC to JR. JR is an investigator of the Howard Hughes Medical Institute.
306 KGH and JR are inventors of MIDAS technology that has been licensed to Atavistik Bio, for which KGH is
307 a consultant and JR is a founder.

308

309 **References**

- 310 1. E. L. Huttlin *et al.*, The BioPlex Network: A Systematic Exploration of the Human Interactome. *Cell*
311 **162**, 425-440 (2015).
- 312 2. D. S. Gilmour, J. T. Lis, Detecting protein-DNA interactions in vivo: distribution of RNA polymerase
313 on specific bacterial genes. *Proc Natl Acad Sci U S A* **81**, 4275-4279 (1984).
- 314 3. D. S. Gilmour, J. T. Lis, In vivo interactions of RNA polymerase II with genes of *Drosophila*
315 *melanogaster*. *Mol Cell Biol* **5**, 2009-2018 (1985).
- 316 4. M. Diether, U. Sauer, Towards detecting regulatory protein-metabolite interactions. *Curr Opin*
317 *Microbiol* **39**, 16-23 (2017).
- 318 5. T. Orsak *et al.*, Revealing the allosterome: systematic identification of metabolite-protein
319 interactions. *Biochemistry* **51**, 225-232 (2012).
- 320 6. L. Chantranupong *et al.*, The CASTOR Proteins Are Arginine Sensors for the mTORC1 Pathway.
321 *Cell* **165**, 153-164 (2016).
- 322 7. R. L. Wolfson *et al.*, Sestrin2 is a leucine sensor for the mTORC1 pathway. *Science* **351**, 43-48
323 (2016).
- 324 8. K. Inoki, Y. Li, T. Xu, K. L. Guan, Rheb GTPase is a direct target of TSC2 GAP activity and regulates
325 mTOR signaling. *Genes Dev* **17**, 1829-1834 (2003).
- 326 9. P. Sun, Y. Liu, T. Ma, J. Ding, Structure and allosteric regulation of human NAD-dependent
327 isocitrate dehydrogenase. *Cell Discov* **6**, 94 (2020).
- 328 10. B. Chaneton *et al.*, Serine is a natural ligand and allosteric activator of pyruvate kinase M2. *Nature*
329 **491**, 458-462 (2012).
- 330 11. R. Lopez-Aleman *et al.*, Inhibition of cell surface mediated plasminogen activation by a monoclonal
331 antibody against alpha-Enolase. *Am J Hematol* **72**, 234-242 (2003).

- 332 12. S. Feo, D. Arcuri, E. Piddini, R. Passantino, A. Giallongo, ENO1 gene product binds to the c-myc
333 promoter and acts as a transcriptional repressor: relationship with Myc promoter-binding protein 1
334 (MBP-1). *FEBS Lett* **473**, 47-52 (2000).
- 335 13. T. Weaver, L. Banaszak, Crystallographic studies of the catalytic and a second site in fumarase C
336 from *Escherichia coli*. *Biochemistry* **35**, 13955-13965 (1996).
- 337 14. K. Nakahigashi *et al.*, Systematic phenome analysis of *Escherichia coli* multiple-knockout mutants
338 reveals hidden reactions in central carbon metabolism. *Mol Syst Biol* **5**, 306 (2009).
- 339 15. S. Galvan-Pena *et al.*, Malonylation of GAPDH is an inflammatory signal in macrophages. *Nat*
340 *Commun* **10**, 338 (2019).
- 341 16. M. Nakano, S. Funayama, M. B. de Oliveira, S. L. Bruel, E. M. Gomes, D-glyceraldehyde-3-
342 phosphate dehydrogenase from HeLa cells--1. Purification and properties of the enzyme. *Comp*
343 *Biochem Physiol B* **102**, 873-877 (1992).
- 344 17. M. Oguchi, E. Gerth, B. Fitzgerald, J. H. Park, Regulation of glyceraldehyde 3-phosphate
345 dehydrogenase by phosphocreatine and adenosine triphosphate. IV. Factors affecting in vivo
346 control of enzymatic activity. *J Biol Chem* **248**, 5571-5576 (1973).
- 347 18. M. Yuan *et al.*, An allostatic mechanism for M2 pyruvate kinase as an amino-acid sensor. *Biochem*
348 *J* **475**, 1821-1837 (2018).
- 349 19. K. Ashizawa, P. McPhie, K. H. Lin, S. Y. Cheng, An in vitro novel mechanism of regulating the
350 activity of pyruvate kinase M2 by thyroid hormone and fructose 1, 6-bisphosphate. *Biochemistry*
351 **30**, 7105-7111 (1991).
- 352 20. S. Hui *et al.*, Glucose feeds the TCA cycle via circulating lactate. *Nature* **551**, 115-118 (2017).
- 353 21. E. K. Wiese *et al.*, Enzymatic activation of pyruvate kinase increases cytosolic oxaloacetate to
354 inhibit the Warburg effect. *Nat Metab* **3**, 954-968 (2021).
- 355 22. G. J. Gowans, D. G. Hardie, AMPK: a cellular energy sensor primarily regulated by AMP. *Biochem*
356 *Soc Trans* **42**, 71-75 (2014).
- 357 23. T. R. Koves *et al.*, Mitochondrial overload and incomplete fatty acid oxidation contribute to skeletal
358 muscle insulin resistance. *Cell Metab* **7**, 45-56 (2008).
- 359 24. D. K. Sindelar *et al.*, The role of fatty acids in mediating the effects of peripheral insulin on hepatic
360 glucose production in the conscious dog. *Diabetes* **46**, 187-196 (1997).
- 361 25. J. Billiard *et al.*, Quinoline 3-sulfonamides inhibit lactate dehydrogenase A and reverse aerobic
362 glycolysis in cancer cells. *Cancer Metab* **1**, 19 (2013).
- 363 26. G. Rai *et al.*, Discovery and Optimization of Potent, Cell-Active Pyrazole-Based Inhibitors of Lactate
364 Dehydrogenase (LDH). *J Med Chem* **60**, 9184-9204 (2017).
- 365 27. G. A. Bezerra *et al.*, Crystal structure and interaction studies of human DHTKD1 provide insight
366 into a mitochondrial megacomplex in lysine catabolism. *IUCrJ* **7**, 693-706 (2020).

- 367 28. G. A. Bezerra *et al.*, Identification of small molecule allosteric modulators of 5,10-
368 methylenetetrahydrofolate reductase (MTHFR) by targeting its unique regulatory domain.
369 *Biochimie* **183**, 100-107 (2021).
- 370 29. Q. Hao *et al.*, Sugar phosphate activation of the stress sensor eIF2B. *Nat Commun* **12**, 3440 (2021).
- 371 30. J. D. Storey, R. Tibshirani, Statistical significance for genomewide studies. *Proc Natl Acad Sci U S*
372 *A* **100**, 9440-9445 (2003).
- 373 31. F. H. Niesen, H. Berglund, M. Vedadi, The use of differential scanning fluorimetry to detect ligand
374 interactions that promote protein stability. *Nat Protoc* **2**, 2212-2221 (2007).
- 375 32. N. Satani *et al.*, ENOblock Does Not Inhibit the Activity of the Glycolytic Enzyme Enolase. *PLoS*
376 *One* **11**, e0168739 (2016).
- 377 33. T. G. Batty, L. Kontogiannis, O. Johnson, H. R. Powell, A. G. Leslie, iMOSFLM: a new graphical
378 interface for diffraction-image processing with MOSFLM. *Acta Crystallogr D Biol Crystallogr* **67**,
379 271-281 (2011).
- 380 34. P. Evans, Scaling and assessment of data quality. *Acta Crystallogr D Biol Crystallogr* **62**, 72-82
381 (2006).
- 382 35. P. R. Evans, G. N. Murshudov, How good are my data and what is the resolution? *Acta Crystallogr*
383 *D Biol Crystallogr* **69**, 1204-1214 (2013).
- 384 36. A. J. McCoy *et al.*, Phaser crystallographic software. *J Appl Crystallogr* **40**, 658-674 (2007).
- 385 37. D. Liebschner *et al.*, Macromolecular structure determination using X-rays, neutrons and electrons:
386 recent developments in Phenix. *Acta Crystallogr D Struct Biol* **75**, 861-877 (2019).
- 387 38. P. Emsley, B. Lohkamp, W. G. Scott, K. Cowtan, Features and development of Coot. *Acta*
388 *Crystallogr D Biol Crystallogr* **66**, 486-501 (2010).
- 389 39. M. A. Ajalla Aleixo, V. L. Rangel, J. K. Rustiguel, R. A. P. de Padua, M. C. Nonato, Structural,
390 biochemical and biophysical characterization of recombinant human fumarate hydratase. *FEBS J*
391 **286**, 1925-1940 (2019).
- 392 40. W. Kabsch, Xds. *Acta Crystallogr D Biol Crystallogr* **66**, 125-132 (2010).
- 393 41. A. Vagin, A. Teplyakov, Molecular replacement with MOLREP. *Acta Crystallogr D Biol Crystallogr*
394 **66**, 22-25 (2010).
- 395 42. G. N. Murshudov, A. A. Vagin, E. J. Dodson, Refinement of macromolecular structures by the
396 maximum-likelihood method. *Acta Crystallogr D Biol Crystallogr* **53**, 240-255 (1997).
- 397 43. C. J. Williams *et al.*, MolProbity: More and better reference data for improved all-atom structure
398 validation. *Protein Sci* **27**, 293-315 (2018).
- 399 44. A. Xiao *et al.*, CasOT: a genome-wide Cas9/gRNA off-target searching tool. *Bioinformatics* **30**,
400 1180-1182 (2014).
- 401 45. A. A. Cluntun *et al.*, The rate of glycolysis quantitatively mediates specific histone acetylation sites.
402 *Cancer Metab* **3**, 10 (2015).

- 403 46. M. J. Lukey *et al.*, Liver-Type Glutaminase GLS2 Is a Druggable Metabolic Node in Luminal-
404 Subtype Breast Cancer. *Cell Rep* **29**, 76-88 e77 (2019).
- 405 47. A. A. Cluntun *et al.*, The pyruvate-lactate axis modulates cardiac hypertrophy and heart failure. *Cell*
406 *Metab* **33**, 629-648 e610 (2021).
- 407 48. J. M. Buescher *et al.*, A roadmap for interpreting (13)C metabolite labeling patterns from cells. *Curr*
408 *Opin Biotechnol* **34**, 189-201 (2015).
- 409 49. J. Qin, G. Chai, J. M. Brewer, L. L. Lovelace, L. Lebioda, Structures of asymmetric complexes of
410 human neuron specific enolase with resolved substrate and product and an analogous complex
411 with two inhibitors indicate subunit interaction and inhibitor cooperativity. *J Inorg Biochem* **111**, 187-
412 194 (2012).

413 **Materials and Methods**

414 MIDAS metabolite library construction and storage

415 The MIDAS metabolite library (Fig. S1A) was constructed by extracting and cross-referencing primary and
416 secondary metabolites from KEGG and HMDB, with a focus on endogenous and exogenous compounds
417 that were quantified, detected, or predicted in human metabolism. All metabolites used in this study were
418 purchased from Sigma-Aldrich, Cayman Chemicals, Avanti Polar Lipids, Enamine, Combi-Blocks, Inc, or
419 custom sourced using Aldrich Market Select (Data S1). Metabolites were solvated to 10 mM in molecular
420 grade water (Sigma-Aldrich W4502) or DMSO (Sigma-Aldrich D1435) and, where necessary to increase
421 solubility, titrated with acid or base. The MIDAS metabolite library was arrayed 1 mL per well in 96-deep
422 well storage plates (Greiner 780280), sealed with aluminum foil seals (VWR 60941-112), and stored at -
423 80°C. When working stocks were needed, metabolites were moved from the deep well storage plates and
424 arrayed, 50 µL per well, across multiple, single-use 384-well small volume plates storage plates (Greiner
425 781280), sealed with aluminum foil seals (VWR 60941-112), and stored at -80°C. Metabolite library
426 management and manipulation was conducted on a Beckman Coulter Biomek NX^P SPAN-8 liquid handling
427 robot.

428

429 MIDAS metabolite library validation and pooling

430 Metabolite accurate mass, adduct, ionization, and detection parameters were determined using a flow
431 injection analysis mass spectrometry (FIA-MS) scouting approach to design four defined metabolite
432 screening pools (Fig. S1B) (Data S2). Briefly, 20 pmol of each metabolite from the MIDAS metabolite library
433 was independently assayed in positive and negative mode in technical quadruplicate 1 µL injections with
434 interspersed blank injections by FIA-MS on a binary pump Agilent 1290 Infinity UHPLC system operated
435 with a flow rate of 0.1 mL/min coupled to an Agilent 6550 ESI-QTOF MS. The following mobile phases were
436 used for FIA-MS scouting: 20 mM formic acid pH 3 (Sigma-Aldrich F0507), 10 mM ammonium acetate pH
437 5 (Sigma-Aldrich 73594), 10 mM ammonium acetate pH 6.8 (Sigma-Aldrich 73594), and 10 mM ammonium
438 bicarbonate pH 9 (Sigma-Aldrich 09830). Source conditions consisted of 250°C gas temp, 11 L/min gas
439 flow, 20 psig nebulizer, 400° sheath gas temperature, 12 L/min sheath gas flow, and 2000 V nozzle voltage.
440 Agilent MassHunter 7 software was used to qualitatively validate and quantify metabolites. The optimal
441 signal for each metabolite was determined by integrating the area under the curve of the extracted ion
442 chromatogram (XIC-AUC) for each metabolite adduct at the various mobile phase pH and instrument
443 polarity. The optimal adduct, pH, polarity, metabolite solvent, and, if necessary, isomer family of each
444 metabolite was considered to construct four unique and defined MIDAS metabolite screening pools (Data
445 S1).

446

447 MIDAS protein-metabolite screening

448 The day of MIDAS screening, a number of MIDAS metabolite library, 384-well small volume working stock
449 plates, corresponding to the number of proteins to be screened (eight proteins per plate), were defrosted

450 at 30°C for 5 minutes and metabolites were combined *de novo* to generate four predetermined MIDAS
451 screening pools (Data S1). The MIDAS screening pools were prepared in LC-MS grade 150 mM ammonium
452 acetate pH 7.4 (Sigma-Aldrich 73594) and pH-adjusted with ammonium hydroxide (Sigma-Aldrich 338818).
453 The majority of metabolites were prepared to a final screening concentration of 50 µM in the metabolites
454 pools, with a subset at higher or lower concentration dependent on their FIA-MS ionization properties (Data
455 S1). For each metabolite pool, 8 µL of target protein (Fig. S1C and Data S3) was arrayed in a minimum of
456 a triplicate across a 10 kDa MWCO 96-well microdialysis plate (SWISSCI Diaplate™) and sealed with
457 aluminum foil seals (Beckman Coulter 538619) to create the protein chambers. To the reverse side, 300
458 µL of metabolite pool was aliquoted per target protein replicate and sealed with aluminum foil seals
459 (Beckman Coulter 538619) to create the metabolite chambers. Where necessary and just prior to screening,
460 proteins provided in alternative buffer systems were *in situ*, sequentially exchanged into 150 mM ammonium
461 acetate pH 7.4 (Sigma-Aldrich 73594) on the 96-well microdialysis screening plate (SWISSCI Diaplate™).
462 Loaded dialysis plates were placed in the dark at 4°C on a rotating shaker (120 rpm) and incubated for 40
463 hours. Post-dialysis, protein and metabolite chamber dialysates were retrieved, sample volume normalized
464 and diluted 1:10 in 80% methanol (Sigma-Aldrich 1060351000) to precipitate protein, incubated 30 mins on
465 ice, and centrifuged at 3200 x g for 15 mins to sequester precipitated protein. Processed protein and
466 metabolite chamber dialysates were retrieved and arrayed across a 384-well microvolume plate (Thermo
467 Scientific AB-1056), sealed with a silicon slit septum cap mat (Thermo Scientific AB-1171), and placed at
468 4°C for FIA-MS analysis.

469

470 MIDAS flow injection analysis mass spectrometry analysis

471 All MIDAS metabolite pool FIA-MS was performed on a Shimadzu Nexera HPLC system equipped with
472 binary LC-20AD_{XR} pumps and a SIL-20AC_{XR} autosampler coupled to a SCIEX X500R ESI-QTOF MS.
473 Briefly, 2 µL of each processed protein and metabolite chamber dialysate (~10 pmoles per metabolite,
474 depending on metabolite) was injected in technical triplicate with blanks injections interspersed between
475 technical replicates. Mobile phase flow rate was 0.2 mL/min. The following mobile phases were used
476 according to the MIDAS metabolite pool being analyzed: pool 1, 5 mM ammonium acetate pH 5 (Sigma-
477 Aldrich 73594), 50% methanol (Honeywell LC230-4); pools 2 and 4, 5 mM ammonium acetate pH 6.8
478 (Sigma-Aldrich 73594), 50% methanol (Honeywell LC230-4); pool 3, 10 mM formic acid pH 3 (Sigma-
479 Aldrich F0507), 50% methanol (Honeywell LC230-4). Pools 1 and 2 were analyzed in positive mode and
480 pools 3 and 4 were analyzed in negative mode. Source conditions consisted of 40 psi for ion source gas 1
481 and 2, 30 psi curtain gas, 600°C source temperature, and +5500 V or -4500 V spray. Method duration was
482 1 min. All target proteins for a given metabolite pool and MS method were analyzed together before
483 switching FIA-MS methods. Between FIA-MS methods, the Shimadzu Nexera HPLC system and SCIEX
484 X500R ESI-QTOF MS were equilibrated for 40 min to the next FIA-MS method. Auto-calibration of positive
485 or negative mode was performed approximately every 45 mins at the beginning of a target protein-

486 metabolite pool batch to control detector drift. Non-dialyzed MIDAS metabolite pools were assayed at the
487 beginning, middle, and end of each metabolite pool method batch to control detector sensitivity.

488

489 MIDAS data processing and analysis

490 MIDAS FIA-MS spectra were processed in SCIEX OS 1.6 software using a targeted method to determine
491 metabolite abundances in the protein chamber and metabolite chamber by integrating the mean area under
492 the curve for each extracted ion chromatogram. If necessary, up to one dialysis replicate per pool per
493 protein was removed if processing or autosampling abnormalities were identified. For each dialysis
494 replicate, $\log_2(\text{fold change})$ for each metabolite was calculated as the difference between the \log_2
495 abundance in the protein chamber and metabolite chamber. $\log_2(\text{fold change})$ for metabolite isomers (e.g.
496 L-Leu/L-Ile/L-Allo-Ile) within the same screening pool were collapsed to a single entry prior to further data
497 processing leading to 333 unique metabolite isomer analytes. Using the replicate protein-metabolite
498 $\log_2(\text{fold change})$ values as input, a processing method was developed in R
499 (<https://github.com/KevinGHicks/MIDAS>) to capture and remove extreme outliers and non-specific
500 systematic variation and to determine significant protein-metabolite interactions. Briefly, for each dialysis
501 replicate set, up to one outlier was removed using a z-score cutoff of five (<0.2% of observations). Technical
502 replicates were then averaged yielding one fold-change summary per protein-metabolite pair. To remove
503 fold-change variation that was not specific to a given protein-metabolite pair, the first three principal
504 components of the total screening dataset were removed on a per metabolite pool basis by subtracting the
505 projection of the first three principal components, creating $\log_2(\text{corrected fold change})$. Protein-metabolite
506 z-scores were determined by comparing the target protein-metabolite $\log_2(\text{corrected fold change})$ to a no-
507 signal model for that metabolite using measures of the central tendency (median) and standard deviation
508 (extrapolated from the inter quartile), which are robust to the signals in the tails of a metabolite's fold-change
509 distribution. Z-scores were false-discovery rate controlled using Storey's q-value (30) and protein-
510 metabolite interactions with q-values < 0.01 were considered significant. Since correcting for non-specific
511 binding, and estimating metabolite-specific standard deviation both benefit from the inclusion of additional
512 proteins, MIDAS data from 122 anonymized proteins were analyzed alongside the 38 proteins specifically
513 considered in this study. The complete MIDAS protein-metabolite interaction dataset for mTORC1
514 regulators and enzymes of central carbon metabolism can be found in Data S4.

515

516 MIDAS proteins

517 All presented proteins analyzed by MIDAS were prepared and provided by collaborators (Data S3) using
518 common protein expression and purification techniques. Proteins were received snap frozen on dry ice
519 from outside sources or on wet ice from local sources. Prior to MIDAS screening, protein quality was
520 assessed by 12.5% SDS-PAGE and concentration was determined by A280 on a NanoDrop One UV-Vis
521 spectrophotometer using the molecular weight and calculated extinction coefficient ($M^{-1} \cdot \text{cm}^{-1}$) of each
522 protein construct. Proteins were screened by MIDAS at the concentrations indicated in Data S3.

523

524 Electrum

525 MIDAS protein-metabolite interaction data for enzymes of central carbon metabolism were visualized for
526 intra- and inter-pathway relationships using Electrum (v0.0.0; <https://github.com/Electrum-app/Electrum>),
527 with q-value cutoff < 0.01, and the 1-D scaling option enabled.

528

529 Differential scanning fluorimetry

530 Thermal differential scanning fluorimetry (DSF) was performed similar to Niesen *et al* (31). Briefly, DSF
531 thermal shift assays were developed to assess protein melting point (T_m) and thermal stability in the
532 presence of putative small molecule ligands: 2-phosphoglycerate (2PG, Sigma-Aldrich 73885),
533 phosphoserine (pSer, Sigma-Aldrich P0878), phosphotyrosine (pTyr, Sigma-Aldrich P9405), phosphate
534 (PO_4 , Acros Organics 424395000), fumarate (Fum, Sigma-Aldrich 47910), 2-amino-3-
535 phosphonopropionic acid (AP-3, Sigma-Aldrich A4910), ATP (Sigma-Aldrich A2383), ADP (Sigma-Aldrich
536 01905), AMP (Sigma-Aldrich A2252), NAD (Sigma-Aldrich N1636), and palmitoyl-CoA (C16:0-CoA,
537 Avanti 870716). Where indicated, DSF experiments were performed using either the standard SYPRO
538 orange fluorescent system or PROTEOSTAT® Thermal shift stability assay kit (ENZO 51027). A final
539 concentration reaction mixture of 10 μ L containing 25mM HEPES pH 7.4, 50mM NaCl, 0.1 mg/mL
540 (SYPRO system) or 0.75 mg/mL (PROTEOSTAT system) target protein, 7.5X SYPRO orange (Sigma-
541 Aldrich S5692) or 1x PROTEOSTAT® reagent, and the indicated concentration of putative ligand was
542 arrayed across a MicroAmp™ optical 384-Well reaction plate (Thermo Scientific 4309849) and sealed
543 with MicroAmp™ optical adhesive film (Thermo Scientific 4360954). Protein denaturation was measured
544 in sextuplicate technical replicates for SYPRO orange and PROTEOSTAT experiments with an excitation
545 of 470 nm and emission of 580 nm on an Applied Biosystems Quantstudio 7 Flex from 25°C to 95°C at a
546 ramp rate of 0.05°C/second. DSF experiments were performed in triplicate. Protein Thermal Shift
547 software 1.4 (Applied Biosystems) was used to interpret and determine protein T_m from the first derivative
548 of the fluorescence emission as a function of temperature (dF/dT). A change in ligand-induced protein
549 melting point (ΔT_m) was determined from the difference of the ligand induced T_m and no-ligand control
550 T_m . Apparent binding affinity (K_{dapp}) was determined by fitting the specific binding and Hill slope
551 equation to ΔT_m as a function of ligand concentration in GraphPad Prism 9 software.

552

553 Fumarase competitive inhibition assay

554 The competitive inhibition of human fumarase activity in the presence of 2-amino-3-phosphonopropionic
555 acid (AP-3, Sigma-Aldrich A4910) was fluorometrically assessed using a coupled enzyme assay. Briefly,
556 the rate limiting hydration of fumarate to malate by fumarase provides substrate, malate, for excess
557 malate dehydrogenase to generate oxalacetate and NADH. Fumarase reaction rate was assessed at
558 room temperature in triplicate with a final reaction volume of 100 μ L composed of 50 mM Tris-HCl pH 9.4,
559 61 μ g/mL human fumarase, excess porcine heart malate dehydrogenase (Sigma-Aldrich 442610-M), 1

560 mM NAD (Sigma-Aldrich N1636), and varying concentrations of fumarate (0 – 40 mM, Sigma-Aldrich
561 47910) and AP-3 (0 – 10 mM, Sigma-Aldrich A4910) (Fig. S2). Fumarate and AP-3 were added
562 simultaneously to initiate the reaction. The production of NADH was quantified fluorometrically in a black,
563 clear bottomed 96-well plate (Sigma-Aldrich CLS3603) on a Biotek Synergy Neo plate reader with 360 nm
564 excitation and 460 nm emission over 10 minutes and fumarase reaction rate was determined from the
565 linear range of increasing NADH signal. A Lineweaver-Burke linear regression and non-linear regression
566 competitive inhibition model of human fumarase between fumarate and AP-3 were fit using GraphPad
567 Prism 9 software from triplicate competitive inhibition experiments.

568

569 Enolase 2 Activity Assay

570 Human enolase 2 (ENO2) activity was measured in the presence of phosphoserine using a coupled
571 enzyme kinetic assay similar to Satani *et al* (32). Briefly, enolase converts 2-phosphoglycerate (2PG) to
572 phosphoenolpyruvate (PEP) and water. Substrate, 2PG, was provided near the measured Km. Excess
573 pyruvate kinase (PK) / lactate dehydrogenase (LDH) enzymes from rabbit muscle (Sigma P0294), ADP,
574 NADH were added to solution to ensure that dehydration of 2PG by enolase was the rate-limiting step.
575 Enolase reaction rate was assessed at room temperature in triplicate with a final reaction volume of 100
576 uL composed of 50 mM HEPES pH 7.4, 0.5 mM MgCl₂, 100 uM NaCl, 1.75 mM ADP, 200 uM NADH,
577 12.8 U PK, 18.4 U LDH, 500 ug ng of ENO2, 30 uM 2PG, with varying concentrations of phosphoserine
578 (pSer). 2PG was used to initiate the coupled enzyme reaction, and the conversion of NADH to NAD by
579 LDH was quantified fluorometrically in a black, clear bottomed 96-well plate (Sigma-Aldrich CLS3603) on
580 a Biotek Synergy Neo plate reader with 360 nm excitation and 460 nm emission over 10 minutes.
581 Enolase reaction rate was determined for the linear range of decreasing NADH signal. IC₅₀ was
582 determined using a sigmoidal, 4PL non-linear regression in Prism 9 from triplicate experiments.

583

584 Enolase X-ray crystallography

585 Crystals of Human Enolase 2 in complex with the phosphoserine ligand were prepared via hanging drop
586 vapor diffusion at 20 °C. 9 mg/ml- Human Enolase 2 protein solution with 2 mM phosphoserine was pre-
587 incubated on ice for 10 min prior to being mixed in 1:1 ratio (protein:reservoir solution) with 100 mM Bis
588 Tris, 200 mM ammonium acetate and 21% (w/v) PEG 3350 at pH 6.5. Orthorhombic crystals grew within
589 3 days and were subsequently cryoprotected with 100 mM Bis Tris, 200 mM ammonium acetate, 32%
590 (w/v) PEG 3350 and 2 mM phosphoserine. X-ray diffraction data were collected at the Advanced Photon
591 Source, synchrotron beamline 22-ID, equipped with Si(III) monochromator and EIGER CCD detector. The
592 diffraction data was processed and integrated using iMOSFLM (33). POINTLESS (34) was used to
593 identify the bravais lattice and space group and AIMLESS (35) was used for scaling. The phase
594 information was obtained by molecular replacement using PHASER (36) with a homodimer of Human
595 Enolase 2 (PDB 4ZCW) as the search model. Iterative cycles of manual model building and refinement

596 were performed within Phenix (37) and COOT (38) software. Diffraction data and refinement statistics are
597 summarized in Table S1.

598

599 Fumarase X-ray crystallography

600 Human fumarase (HsFH) was produced and purified as previously described (39). The co-crystallization
601 experiments were carried out by using the sitting drop method. Protein solution (4 mg/mL in 50 mM Tris-
602 HCl (Sigma-Aldrich), pH 8.5, 150 mM KCl (J.T.Baker) was incubated with 20 mM of D-2-amino-3-
603 phosphono-propionic acid (AP-3). 2 μ L of protein solution was mixed with 2 μ L of reservoir solution, and
604 allowed to equilibrate against 500 μ L of reservoir solution at 21°C. Crystals occur over the course of 3
605 days in drops where the reservoir contained 100 mM Hepes pH 7.5 (Sigma-Aldrich), 1% v/v 2-
606 methylpentanediol (MPD) (Sigma-Aldrich) and 18% (w/v) PEG 10 K (Sigma-Aldrich) and 25% (v/v)
607 glycerol. Prior to data collection, HsFH crystals were soaked in a cryoprotectant solution (100 mM Hepes
608 pH 7.5, 1% v/v 2-methylpentanediol (MPD), and 18% m/v PEG 10 K, 25% v/v glycerol (Labsynth),
609 harvested with cryo loops, and flash-cooled in liquid nitrogen. The data set was collected at 100 K on a
610 synchrotron facility (MANACA beamline - SIRIUS, Brazil) using a PILATUS 2M detector (Dectris). 3600
611 frames with an oscillation step of 0.1° were collected using an exposure time of 0.1 s per image with a
612 crystal-to-detector distance of 120.05 mm. The images of X-ray diffraction were processed with XDS (40)
613 package, and the structure of HsFH was solved by molecular replacement implemented in Molrep (41)
614 program, and using the human fumarase structure (PDB ID: 5UPP) (39) as a template. The structure was
615 refined with Refmac5 (42) intercepted with manual map inspection and model building using Coot (38).
616 The quality of the model was regularly checked using MolProbity (43). Diffraction data and refinement
617 statistics are summarized in Table S2. The refined atomic coordinates and structure factors were
618 deposited in the PDB with the accession code 7LUB.

619

620 Lactate dehydrogenase activity assay

621 Human lactate dehydrogenase A (LDHA) and lactate dehydrogenase B (LDHB) activity were assessed in
622 the presence of putative nucleotide and fatty acyl-CoA derivatives using a standard NADH fluorometric
623 assay. Briefly, lactate dehydrogenase reversibly converts lactate and NAD to pyruvate and NADH. With
624 the exception of the competitive inhibition assay, LDHA and LDHB activity assays were operated near
625 their measured substrate and cofactor K_m . Lactate dehydrogenase reaction rate was assessed at room
626 temperature in triplicate with a final reaction volume of 100 μ L composed of 75 mM Tris pH 7.4, 67.2
627 ng/ml LDHA or 75 ng/mL LDHB, 6.5 mM Lactate (Sigma-Aldrich L6402) and 200 μ M NAD (Sigma-Aldrich
628 N1636) for LDHA and 1mM lactate and 1.25 mM NAD for LDHB, with varying concentrations of putative
629 ligand, as indicated: ATP (Sigma-Aldrich A2383), ADP (Sigma-Aldrich 01905), AMP (Sigma-Aldrich
630 A2252), CoA (Avanti 870701), C2:0-CoA (Avanti 870702), C4:0-CoA (Avanti 870704), C8:0-CoA (Avanti
631 870708), C12:0-CoA (Avanti 870712), C16:0-CoA (Avanti 870716), C18:1-CoA (Avanti 870719), and
632 C20:0-CoA (Avanti 870720). For competitive inhibition assay, the concentrations of lactate or NAD were

633 varied, accordingly. In all circumstances, NAD was used to initiate the lactate dehydrogenase reaction.
634 The production of NADH was quantified fluorometrically in a black, clear bottomed 96-well plate (Sigma-
635 Aldrich CLS3603) on a Biotek Synergy Neo plate reader with 360 nm excitation and 460 nm emission
636 over 10 minutes and lactate dehydrogenase reaction rate was determined from the linear range of
637 increasing NADH signal. IC₅₀ were determined using a sigmoidal, 4PL non-linear regression in Prism 9
638 from triplicate experiments. Non-linear regression competitive or non-competitive inhibition modeling of
639 LDHA between lactate or NAD and ATP or palmitoyl-CoA were fit using GraphPad Prism 9 software from
640 triplicate experiments.

641

642 Palmitoyl-CoA-Agarose pull-down assay

643 LDHA and LDHB interaction with palmitoyl-CoA was assessed using a pull-down, competitive elution
644 assay. Briefly, 30 µL per pull-down of palmitoyl-CoA conjugated agarose beads (Sigma-Aldrich 5297)
645 were buffer exchanged into pull-down buffer (75mM Tris HCl pH 7.4). In a final volume of 300 µL, 0.2
646 mg/mL of LDHA or LDHB protein were combined with buffer exchanged palmitoyl-CoA agarose beads, a
647 loading control was saved, and the mixture was incubated overnight at 4°C with gentle agitation. Post-
648 incubation, pull-down reactions were washed 5x in 100 µL of pull-down buffer and the final wash was
649 saved for analysis. Following the fifth wash, 100 µM of acetyl-CoA or palmitoyl-CoA or equivalent volume
650 of pull-down buffer were added to the reactions and incubated overnight at 4°C. In the morning, the pull-
651 down reactions were centrifuged to pellet beads, the supernatant was collected and concentrated as the
652 eluate fraction, the beads were collected as the bound fraction, and all samples were boiled for 5 minutes
653 in 4x Laemmli sample buffer and analyzed by SDS-PAGE for presence of LDHA or LDHB.

654

655 Tissue culture

656 H9c2 myoblastic cell line (ATCC CRL-1446) was purchased from ATCC and routinely maintained in
657 DMEM media supplemented with 10% FBS and 1% PenStrep in 5% CO₂ and 37°C.

658

659 *Ldha* and *Ldhb* mutant cell lines

660 *Ldha* and *Ldhb* knock out H9c2 cell lines were generated using CRISPR-Cas9 to excise the first coding
661 exon of each gene. Single guide modified synthetic sgRNAs were obtained from Synthego and Hifi-Cas9
662 was obtained from IDT (cat# 1081060). Pairs of ribonucleoprotein (RNP) complexes targeting upstream
663 and downstream of the first coding exon for each gene were co-electroporated using a Lonza 4D
664 Nucleofector system (<https://knowledge.lonza.com/cell?id=1016&search=H9c2>). The N20 sgRNA target
665 sequences used were GAGTGCAACGCTCAACGCCA and TCCACAGGCTTGTGACATAA for *Ldha* and
666 TCCATGCATGTAAAGCACAT and AAGACAGCACAACCTCTATAG for *Ldhb*. Off-targets for these
667 sgRNAs were screened using CasOT (44). Nucleofected cells were plated as single clones and clones
668 were screened for the expected genomic deletion and presence of the WT allele using PCR and these
669 results were confirmed using Western blotting.

670

671 Cell lysate and western blotting

672 Harvested cells were washed with PBS and lysed in RIPA buffer (50 mM Tris, 150 mM NaCl, 0.1% SDS,
673 0.5% sodium deoxycholate, 1% NP-40) supplemented with protease and phosphatase inhibitors. Protein
674 concentration was quantified with the Pierce BCA Protein Assay Kit. Samples were mixed with 4x sample
675 loading buffer and incubated for 5 min at 95°C. 30 µg of total protein lysate was resolved on SDS
676 polyacrylamide gel according to standard procedure at 20 mA per gel and blotted onto a nitrocellulose
677 membrane 0.45 µm (GE Healthcare) via Mini Trans-blot module (Bio-Rad) at a constant voltage (100 V) for
678 2 h. After blocking with 5% non-fat milk (Serva)/Tris-buffered saline with 0.05% Tween 20 (TBS-T) for 1 h,
679 the membrane was incubated overnight in 5% bovine serum albumin (Sigma-Aldrich), TBS-T with primary
680 antibody against LDHA (Cell Signaling Technology 2012S, 1:1000), LDHB (Abcam ab240482, 0.1 g/ml),
681 and GAPDH (Cell Signaling Technology 97166, 1:1000). Next day, the membrane was washed with TBS-
682 T and incubated with corresponding fluorophore-conjugated secondary antibody (Rockland
683 Immunochemical RL611-145-002, 1:10000) in 1% non-fat milk/TBS-T for 1 h. The membrane was then
684 washed again with TBS-T and fluorescence was assessed with Odyssey CLx imaging system (LI-COR
685 Biosciences).

686

687 Metabolite extraction

688 The procedures for metabolite extraction from cultured cells are described in previous studies (45-47).
689 Briefly, adherent cells were grown in 10 cm plates in biological triplicate to 80% confluence, medium was
690 rapidly aspirated and cells were washed with cold 0.9% NaCl TC grade (Sigma-Aldrich S8776-100ML) on
691 ice. 3 mL of extraction solvent, 80% (v/v) LC/MS grade methanol/water (Fisher Scientific W6-1, A456-1)
692 cooled to -80°C, was added to each well, and the dishes were transferred to -80°C for 15 min. Cells were
693 then scraped into the extraction solvent on dry ice. Additionally, 300mL of media was collected and
694 processed from each sample pre and post experiment. All metabolite extracts were centrifuged at 20,000
695 x g at 4°C for 10 min. Each sample was transferred to a new 1.5 mL tube. Finally, the solvent in each
696 sample was evaporated in a Speed Vacuum, and stored at -80°C until they were run on the mass
697 spectrometer.

698

699 [U-13C6]-Glucose and [U-13C3]-Lactate labeling with or without palmitate

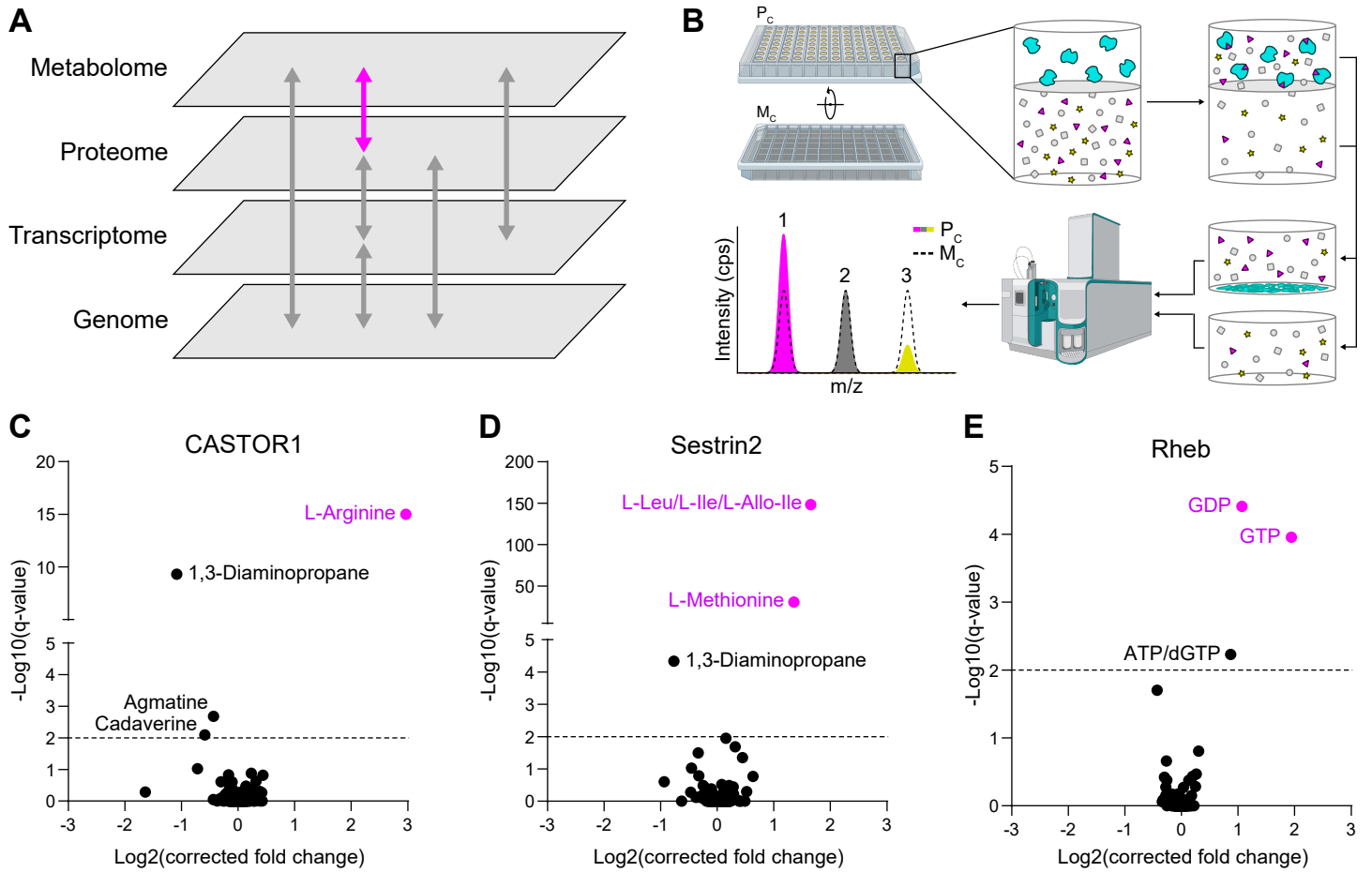
700 Cells were grown to 80% confluence in 10 cm plates with standard culture medium at which point 10 µM of
701 the MPC inhibitor UK5099 (Sigma-Aldrich PZ0160-5MG) was added for 48 hours to facilitate lactate
702 production. Cells were subsequently washed with sterile PBS and either free BSA or BSA conjugated to
703 palmitate (Caymen Chemical 29558) was added to culture media containing either [U-13C6]-L-glucose, or
704 [U-13C3]-L-lactate (Cambridge Isotope Laboratories CLM-1396, CLM-1579-PK), supplemented with
705 dialyzed Fetal Bovine Serum (Thermo Scientific A3882001) and incubated for 4 hours. Metabolites were
706 extracted as described above. Data was corrected for naturally occurring 13C isotope abundance before

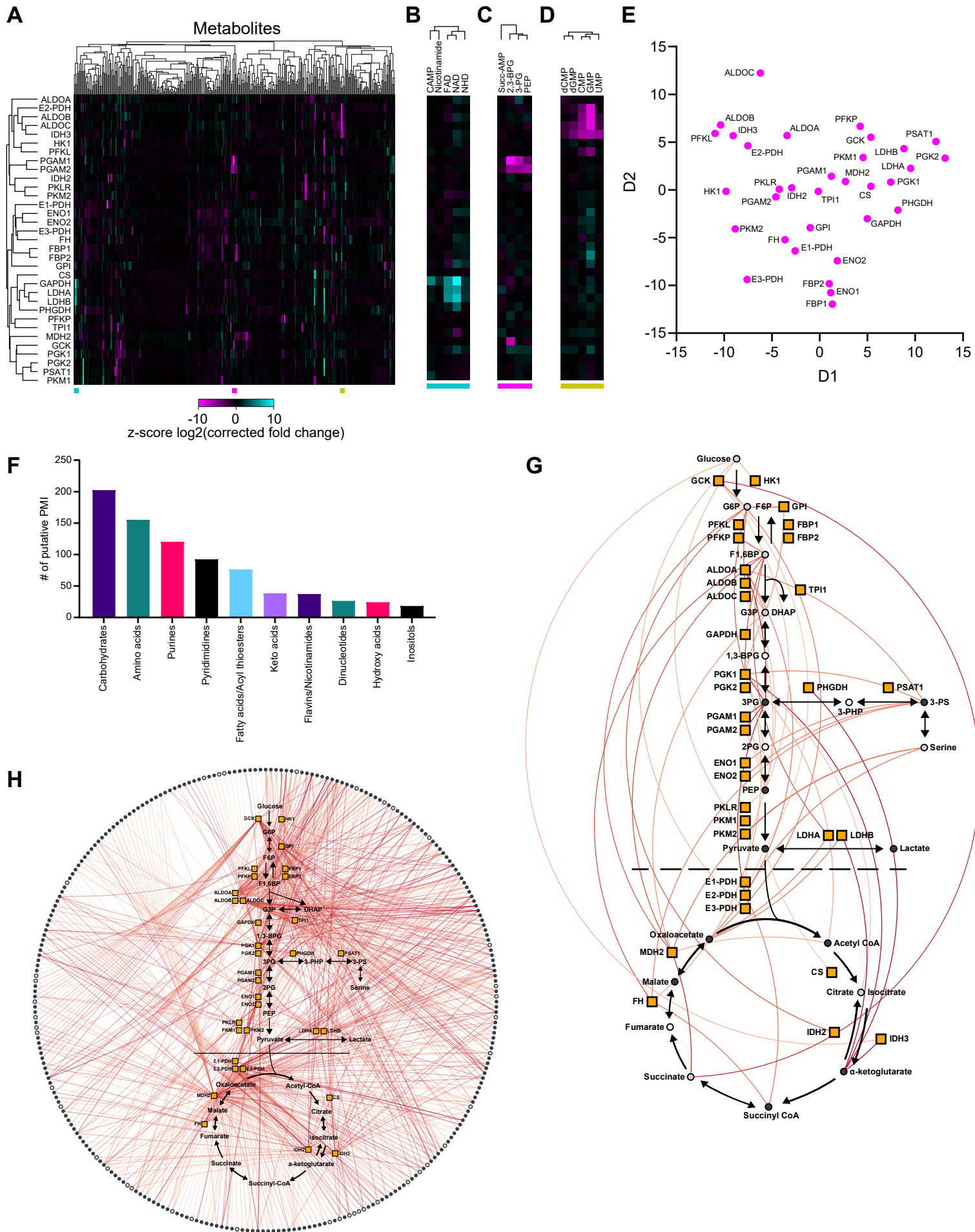
707 analysis as described in Buescher *et al* (48). All data expressed as mean \pm SD unless otherwise indicated.
708 Student's t test was used for 2 group comparison. One-Way ANOVA and Sidak's comparisons were used
709 for multigroup comparison. $p < 0.05$ were considered statistically significant. Statistical analyses and
710 graphics were carried out with GraphPad Prism 9 software.

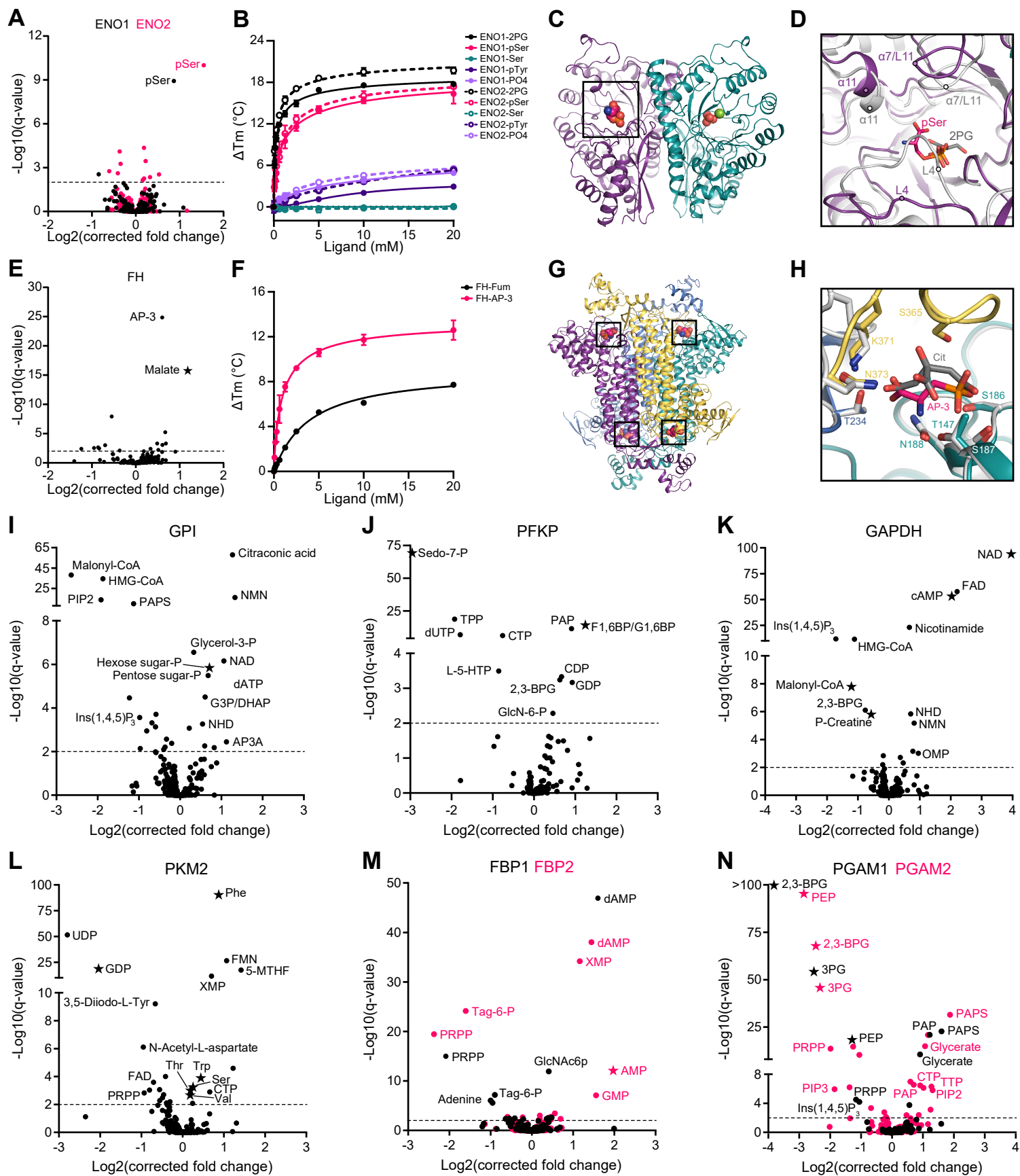
711

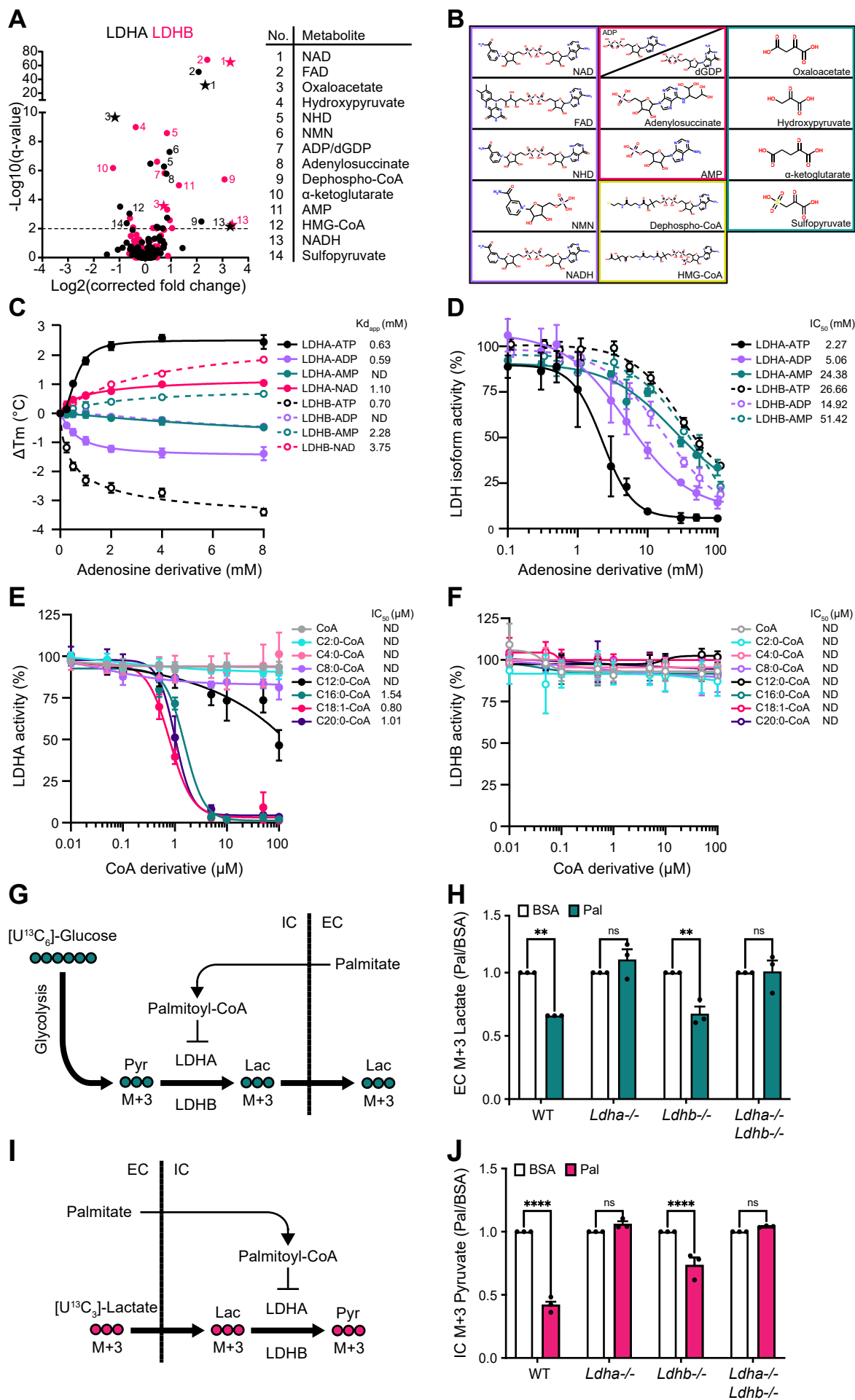
712 Metabolomic analysis

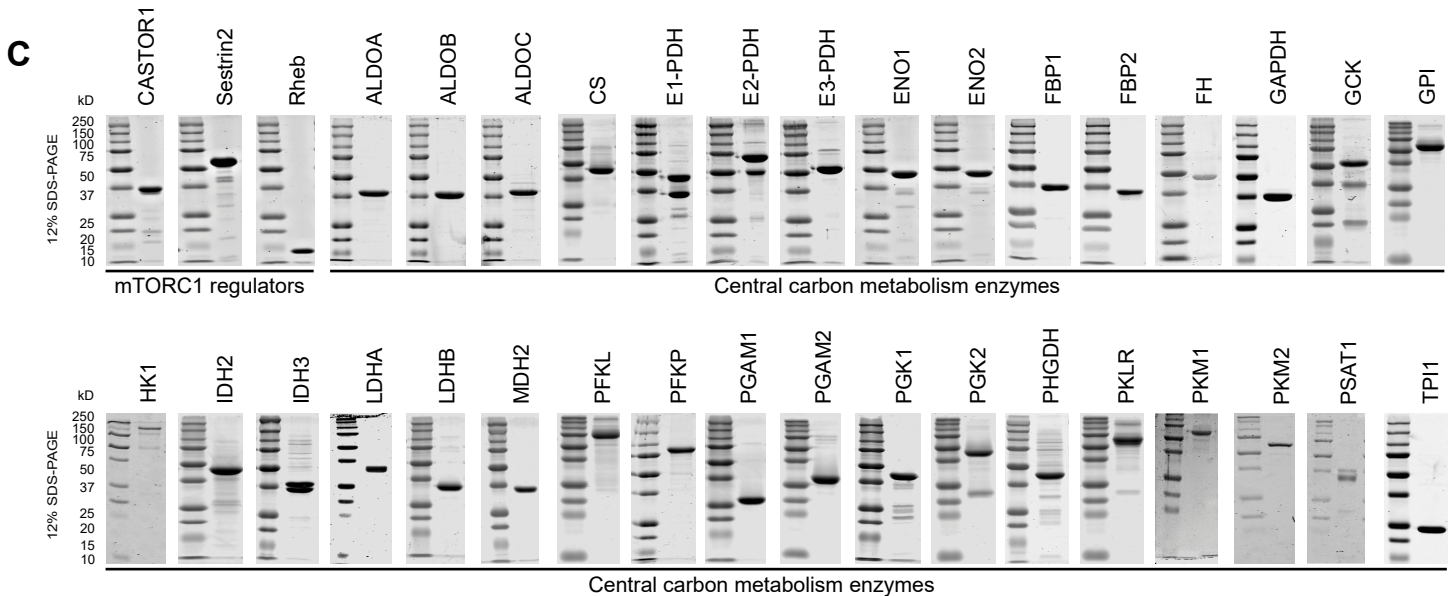
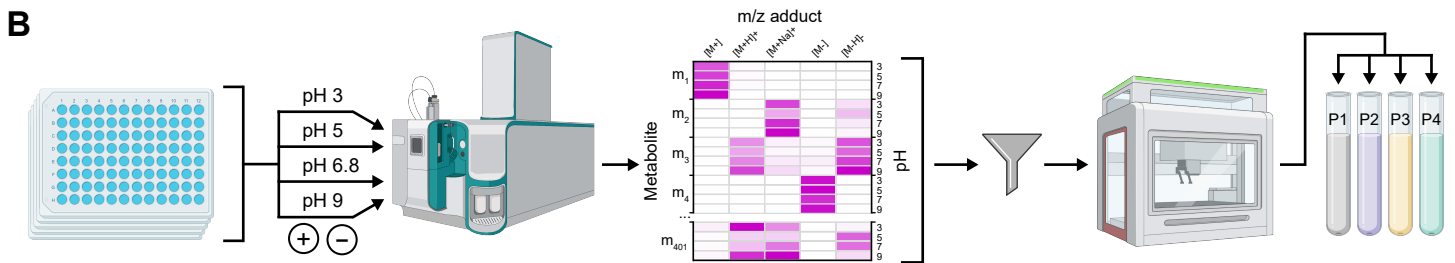
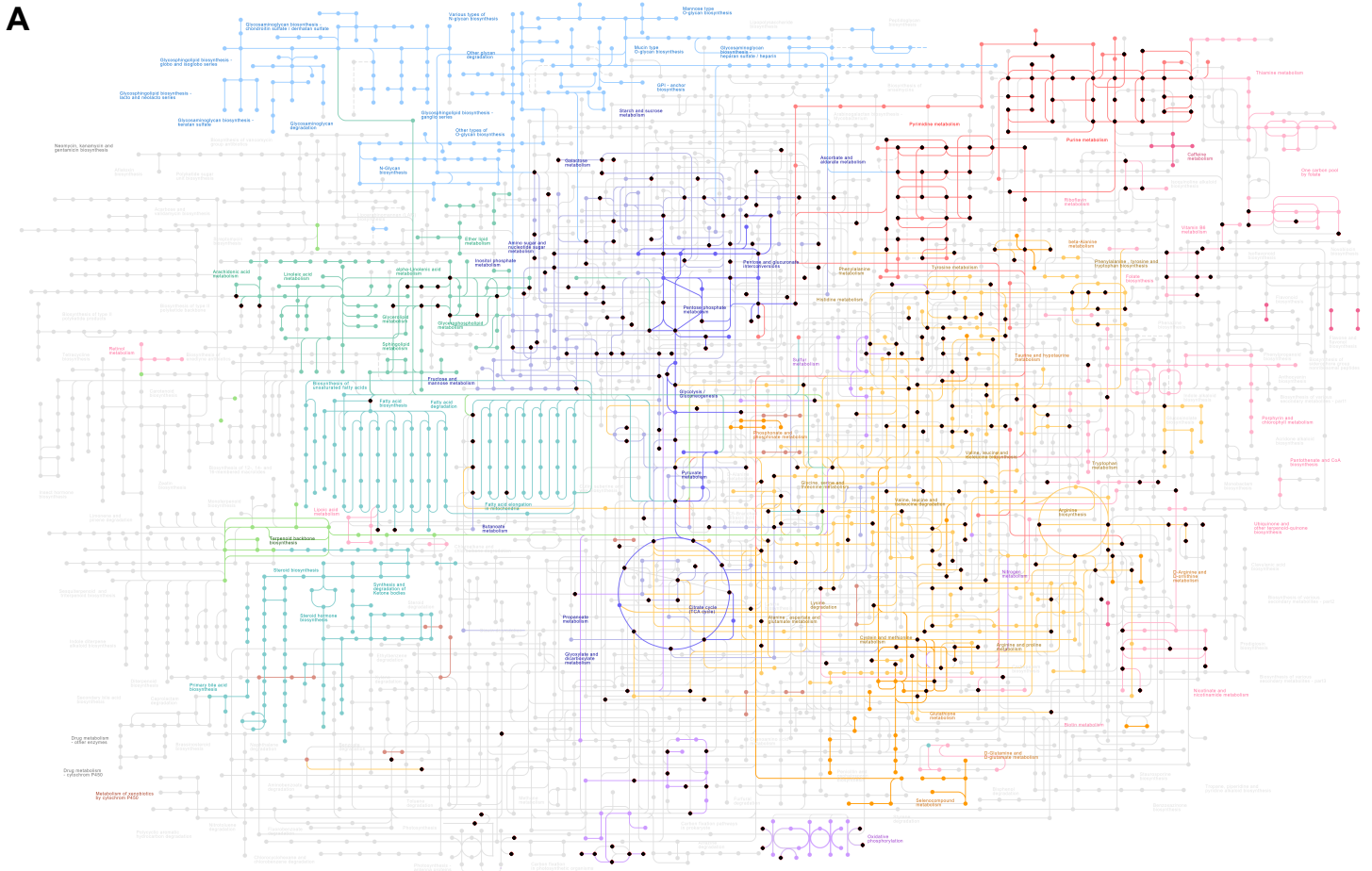
713 The levels of metabolites in the H9c2 cells were measured by gas chromatography–mass spectroscopy
714 (GC-MS) analysis. All GC-MS analysis was performed with a Waters GCT Premier mass spectrometer
715 fitted with an Agilent 6890 gas chromatograph and a Gerstel MPS2 autosampler. Dried samples were
716 suspended in 40 μ L of a 40 mg/mL O-methoxylamine hydrochloride (MOX) in pyridine and incubated for 1
717 h at 30°C. 10 μ L of N-methyl-N-trimethylsilyltrifluoroacetamide (MSTFA) was added automatically via the
718 autosampler and incubated for 60 min at 37°C with shaking. After incubation 3 μ L of a fatty acid methyl
719 ester standard solution was added via the autosampler. Then 1 μ L of the prepared sample was injected to
720 the gas chromatograph inlet in the split mode with the inlet temperature held at 250°C. A 10:1 split ratio
721 was used for analysis. The gas chromatograph had an initial temperature of 95°C for one minute followed
722 by a 40°C/min ramp to 110°C and a hold time of 2 min. This was followed by a second 5°C/min ramp to
723 250°C, a third ramp to 350°C, then a final hold time of 3 min. A 30 m Phenomex ZB5-5 MSi column with a
724 5 m long guard column was employed for chromatographic separation. Helium was used as the carrier gas
725 at 1 mL/min. Data was extracted from each chromatogram as area under the curve for individual
726 metabolites. Each sample was first normalized to the added standard d4-succinate to account for extraction
727 efficiency followed by normalization to cell number. Due to this being a broad scope metabolomics analysis,
728 no normalization for ionization efficiency or concentration standards was performed.

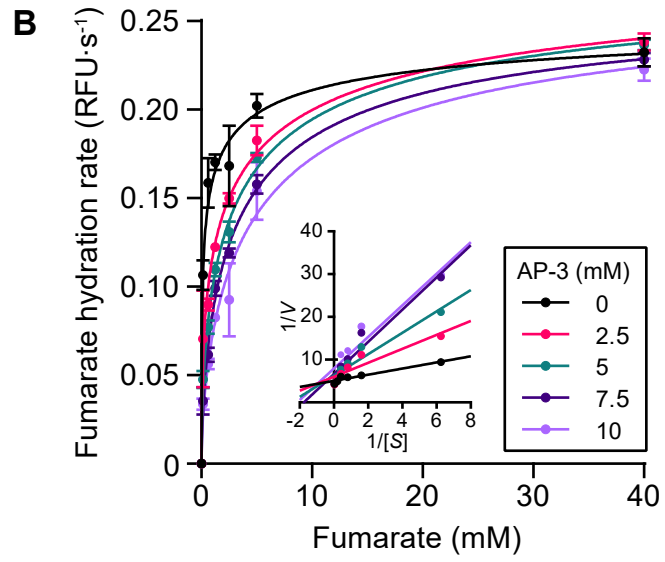
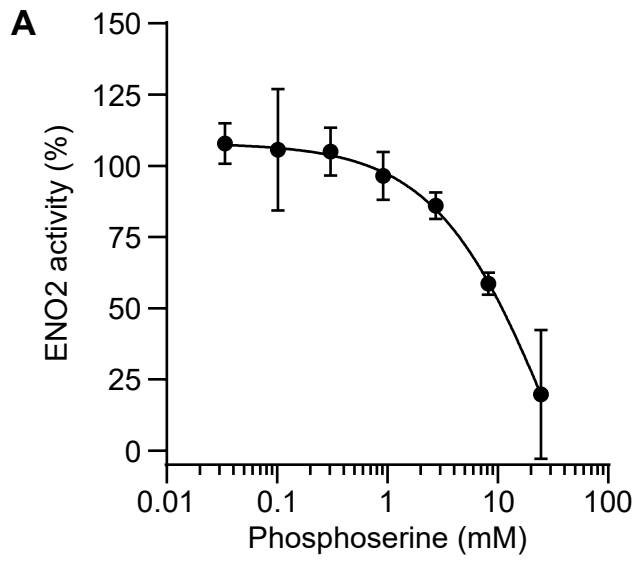












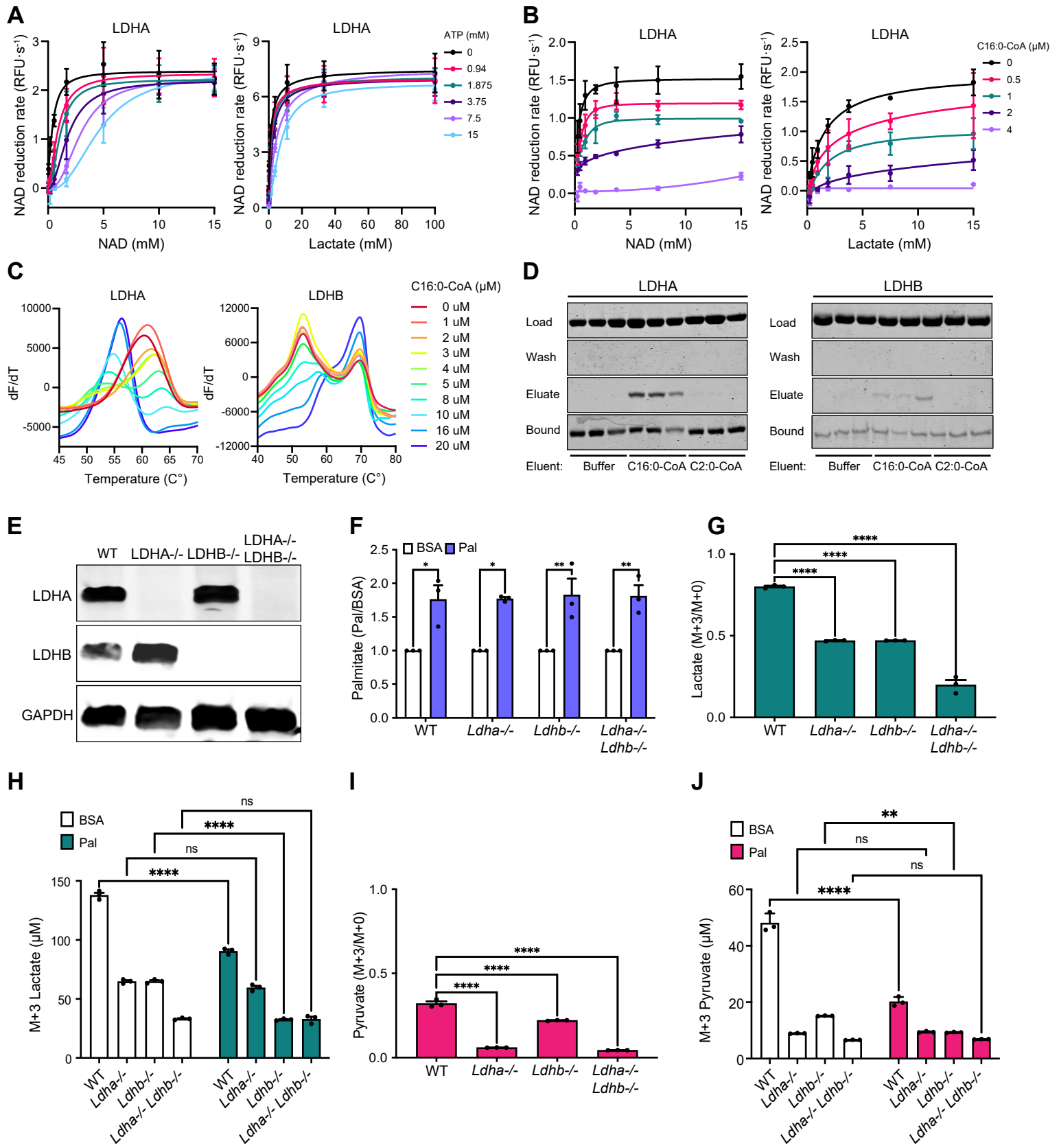
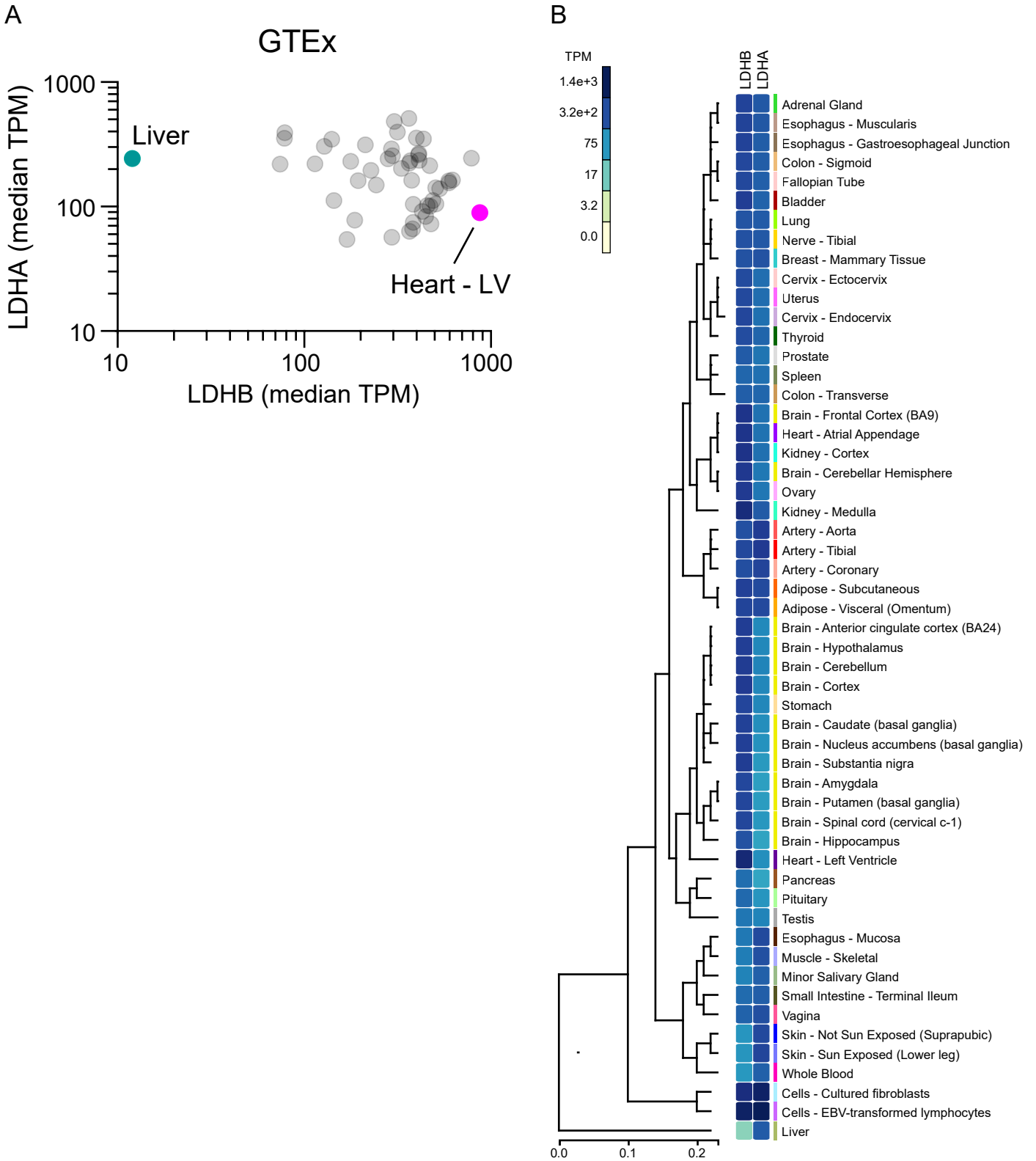


Fig. S4



729 **Figure Legends**

730 **Figure 1. MIDAS is a platform for the systematic discovery of protein-metabolite interactions.**

731 **(A)** Biological systems are organized into domains of information (panes). Movement and interaction of
732 information in and through these domains underlies biological function (arrows). The MIDAS platform
733 provides protein-metabolite interactome (purple arrow) discovery. **(B)** The MIDAS platform is an equilibrium
734 dialysis tandem mass spectrometry approach. (Top) Purified proteins (cyan) are loaded into the protein
735 chamber (P_c) and defined pools of metabolites into the metabolite chamber (M_c), separated by a protein-
736 impermeable membrane. The system is incubated to relative equilibrium. (Bottom) Proteins are removed,
737 the P_c and M_c are sampled, and the relative abundance of metabolites from each chamber are quantified
738 using FIA-MS. Interactions between proteins and metabolites are observed as an increase (1, magenta) or
739 decrease (3, yellow) in integrated signal intensity in the P_c relative to the M_c (dotted peak). Metabolites that
740 have equal integrated signal intensity in the P_c relative to the M_c (2, grey) are defined as non-interacting.
741 **(C, D, E)** The mTORC1 regulators CASTOR, Sestrin2, and Rheb were screened using MIDAS. Known
742 metabolite regulators are highlighted (magenta). Significant protein-metabolite interactions have a q-value
743 < 0.01 (dotted line).

744

745 **Figure 2. The protein-metabolite interactome of human central carbon metabolism.**

746 **(A)** Heatmap representation of the MIDAS protein-metabolite interactomes of 33 enzymes in central carbon
747 metabolism. Heatmap values are the z-score $\log_2(\text{corrected fold change})$ for all metabolites in the MIDAS
748 metabolite library on a per protein basis. Clustering was performed by one minus Pearson correlation.
749 Positive (cyan) and negative (magenta) metabolite z-score $\log_2(\text{corrected fold change})$ have a maximum
750 and minimum cut-off of 10 and -10 , respectively. **(B, C, D)** Excerpt examples of metabolite clustering from
751 (A). Colored bars (bottom) indicate the location of the extracted heatmaps from (A) (bottom). **(E)**
752 Multidimensional scaling (MDS) of 33 enzymes in central carbon metabolism based on their MIDAS protein-
753 metabolite interactomes. MDS distance values were generated from the z-score $\log_2(\text{corrected fold}$
754 $\text{change})$ for all metabolites in the MIDAS metabolite library on a per protein basis. **(F)** The top ten metabolite
755 sub-classes by total protein-metabolite interaction (PMI) count across 33 enzymes in human central carbon
756 metabolism. Metabolite sub-classes were modified from HMDB chemical taxonomy sub-class. **(G and H)**
757 Significant intra-pathway (G) and inter-pathway (H) interactions (colored lines) between metabolites (black
758 circles) and 33 enzymes in central carbon metabolism (orange boxes) detected by MIDAS (plots generated
759 in *Electrum*). Unique metabolites (dark grey circles), metabolite isoforms (light grey circles), metabolites not
760 present in the library (open circles). Significant protein-metabolite interactions have a q-value < 0.01 and
761 are colored by increasing significance, light orange to red.

762

763 **Figure 3. MIDAS reveals known and novel metabolite interactions with enzymes from human central** 764 **carbon metabolism.**

765 **(A)** Metabolite interactions with enolase 1 (ENO1, black) and enolase 2 (ENO2, pink). **(B)** Ligand-induced
766 DSF melting point analysis of ENO1 (solid lines, solid circles) and ENO2 (dotted lines, open circles) with 2-
767 phosphoglycerate (2PG, black), phosphoserine (pSer, pink), serine (Ser, teal), phosphotyrosine (pTyr,
768 purple), and phosphate (PO₄, light purple). **(C)** X-ray crystal structure of the pSer-ENO2 complex (PDB
769 7MBH). pSer (black box), phosphate ion (orange and red spheres), magnesium ion (green sphere),
770 monomers within the ENO2 dimer (purple and teal). **(D)** Magnified view of the ENO2 active site with pSer
771 (pink) or 2-phosphoglycerate (2PG) (grey) bound (2PG-ENO2, PDB 3UCC) (49). Secondary structure
772 labeled in the pSer-ENO2 (purple) and 2PG-ENO2 (light grey) structures. **(E)** Metabolite interactions with
773 fumarase (FH). **(F)** Ligand-induced DSF melting point analysis of FH with fumarate (Fum, black) and 2-
774 Amino-3-phosphonopropionic acid (AP-3, pink). **(B and F)** Line of best fit was determined using the specific
775 binding and Hill slope equation from Prism 9. **(G)** X-ray crystal structure of the AP-3-FH complex (PDB
776 7LUB). AP-3 (black boxes), monomers within the FH tetramer (purple, yellow, teal, and light blue). **(H)**
777 Magnified view of the FH active site with AP-3 (pink) or citrate (Cit, grey) bound (*E. coli* Cit-FH structure,
778 light grey, PDB 1FUO) (13). Sidechains that coordinate the AP-3 interaction with FH are labeled and colored
779 according to FH monomer from (G). **(I)** Metabolite interactions with glucose-6-phosphate isomerase (GPI).
780 **(J)** Metabolite interactions with 6-Phosphofructokinase, platelet type (PFKP). **(K)** Metabolite interactions
781 with glyceraldehyde-3-phosphate dehydrogenase (GAPDH). **(L)** Metabolite interactions with pyruvate
782 kinase M2 (PKM2). **(M)** Metabolite interactions with fructose-1,6-bisphosphatase 1 (FBP1, black) and
783 fructose-1,6-bisphosphatase 2 (FBP2, pink). **(N)** Metabolite interactions with phosphoglycerate mutase 1
784 (PGAM1, black) and phosphoglycerate mutase 2 (PGAM2, pink). **(A, E, I – N)** Volcano plots generated from
785 MIDAS PMI data. Specific metabolites are labeled. Stars indicate a previously known human PMI primarily
786 sourced from BRENDA (<https://www.brenda-enzymes.org/index.php>). Significant protein-metabolite
787 interactions have a q-value < 0.01 (dotted line).

788
789 **Figure 4. ATP and long-chain acyl-CoAs inhibit lactate dehydrogenase in an isoform-specific**
790 **manner.**

791 **(A)** Metabolite interactions with lactate dehydrogenase A (LDHA, black) and lactate dehydrogenase B
792 (LDHB, pink). Volcano plots generated from MIDAS PMI data. Specific metabolites are numbered and
793 labeled. Stars indicate a previously known human PMI primarily sourced from BRENDA
794 (<https://www.brenda-enzymes.org/index.php>). Significant protein-metabolite interactions have a q-value <
795 0.01 (dotted line). **(B)** Metabolite classes that interact with LDHA and LDHB from (A) (nicotinamides and
796 dinucleotides, purple; adenosine nucleotide derivatives, pink; coenzyme A derivatives, yellow; keto acids,
797 teal). **(C)** Ligand-induced DSF melting point analysis of LDHA (solid lines, filled circles) and LDHB (dotted
798 lines, open circles) with adenosine triphosphate (ATP, black), adenosine diphosphate (ADP, light purple),
799 adenosine monophosphate (AMP, teal), and nicotinamide adenine dinucleotide (NAD, pink). Apparent
800 dissociation constant (K_{dapp}) was determined from triplicate experiments using the specific binding and Hill
801 slope equation from Prism 9. Mean \pm SD is plotted from triplicate experiments. **(D)** Enzyme activity of LDHA

802 (solid lines, filled circles) and LDHB (dotted lines, open circles) treated with ATP (black), ADP (light purple),
803 or AMP (teal). **(E and F)** Enzyme activity of LDHA or LDHB treated with coenzyme A (CoA, grey), acetyl-
804 CoA (C2:0-CoA, cyan), butyryl-CoA (C4:0-CoA, light pink), octanoyl-CoA (C8:0-CoA, light purple), lauroyl-
805 CoA (C12:0-CoA, black), palmitoyl-CoA (C16:0-CoA, teal), oleoyl-CoA (C18:1-CoA, pink), and saturated
806 arachidonoyl-CoA (C20:0-CoA, purple). **(D – F)** Half maximal inhibitory concentration (IC_{50}) was determined
807 from triplicate experiments using Prism 9; ND, not determined. Mean \pm SD is plotted from triplicate
808 experiments. **(G)** Schematic of [$U^{13}C_6$]-glucose metabolism in cells treated with palmitate-conjugated BSA.
809 Pyruvate, Pyr; lactate, Lac; IC, intracellular; EC, extracellular. **(H)** Fold change of extracellular [$U^{13}C_3$]-
810 lactate collected from the growth media of the indicated H9c2 cell lines in response to treatment with
811 palmitate-conjugated BSA (Pal) relative to BSA control. **(I)** Schematic of [$U^{13}C_3$]-lactate metabolism in cells
812 treated with palmitate-conjugated BSA. Pyruvate, Pyr; lactate, Lac; IC, intracellular; EC, extracellular. **(J)**
813 Fold change of intracellular [$U^{13}C_3$]-pyruvate in indicated H9c2 cell lines in response to treatment with
814 palmitate-conjugated BSA (Pal) relative to BSA control. **(H and J)** Experiments were performed in triplicate
815 and mean \pm SD is displayed. A students t-test was performed between Pal and BSA samples ($p < 0.005$,
816 **, $p < 0.00005$, ****).

817

818 Supplemental Figure Legends

819 Figure S1. MIDAS metabolite library construction and validation and screened proteins.

820 **(A)** The MIDAS metabolite library overlaid on KEGG human metabolic pathways
821 (<https://www.genome.jp/kegg/pathway/map/map01100.html>). Human pathways, colored; non-human
822 pathways, light grey. Metabolites from the MIDAS metabolite library, black spheres. **(B)** FIA-MS scouting
823 method to determine optimal MIDAS metabolite pools. Metabolites from the MIDAS metabolite library were
824 arrayed across five 96-well plates in water. Each metabolite was individual analyzed at mobile phase pH 3,
825 5, 6.8, and 9, in positive and negative mode, by FIA-MS. For each metabolite ($m_1 - m_{401}$) analyzed by FIA-
826 MS, accurate mass was verified and optimal signal was determined from the integrated area under the
827 curve for the extracted ion chromatogram of each metabolite adduct, mobile phase pH, and polarity
828 (increasing FIA-MS signal, white to magenta Heatmap). The optimal FIA-MS signal conditions of each
829 metabolite were manually filtered and binned to program an automated liquid handling method to construct
830 the MIDAS metabolite pools (P1, P2, P3, and P4) according to the specific conditions of metabolite analysis
831 by FIA-MS. **(C)** SDS-PAGE analysis of the purified proteins analyzed by MIDAS. mTORC1 regulators and
832 the enzymes from central carbon metabolism are labeled.

833

834 Figure S2. Enzymatic activities of enolase and fumarase with interacting metabolites.

835 **(A)** Activity of enolase, expressed as a percentage of vehicle control, was determined in the presence of
836 varying concentrations of phosphoserine (pSer) using a coupled enzyme kinetic assay with pyruvate
837 kinase/lactate dehydrogenase. The experiment was performed in triplicate and the mean \pm SD are plotted.

838 **(B)** Relative fumarate hydration rate by fumarase was determined in the presence of varying concentrations
839 of substrate, fumarate, and the inhibitor, 2-amino-3-phosphonopropionic acid (AP-3, colored) using a
840 malate dehydrogenase coupled enzyme assay. (Inset) Lineweaver–Burk plot demonstrating competitive
841 inhibition. The experiment was performed in triplicate and the mean \pm SD are plotted.

842

843 **Figure S3. Lactate dehydrogenase interacts with and is inhibited by nucleotides and long-chain**
844 **acyl-CoA.**

845 **(A)** Relative NAD reduction rate by LDHA was determined in the presence of varying concentrations of
846 NAD (cofactor) or lactate (substrate), and ATP (colored) using a lactate dehydrogenase enzyme assay.
847 The experiments were performed in triplicate and the mean \pm SD are plotted. **(B)** Relative NAD reduction
848 rate by LDHA was determined in the presence of varying concentrations of NAD (cofactor) or lactate
849 (substrate), and palmitoyl-CoA (C16:0-CoA) (colored) using a lactate dehydrogenase enzyme assay. The
850 experiments were performed in triplicate and the mean \pm SD are plotted. **(C)** LDHA and LDHB were
851 analyzed by PROTEOSTAT DSF in the presence of increasing concentrations of C16:0-CoA (colored).
852 dF/dT was determined as a function of temperature. Representative experiments from triplicate
853 experiments are presented. **(D)** Palmitoyl-CoA-Agarose pull-down assay with LDHA or LDHB treated with
854 buffer control, palmitoyl-CoA (C16:0-CoA), or acetyl-CoA (C2:0-CoA) (Eluent). Protein input (Load), post-
855 5x wash (Wash), concentrated supernatant post-eluent treatment (Eluate), protein bound to palmitoyl-CoA-
856 agarose beads post-eluent treatment (Bound). The experiment was performed in triplicate. **(E)**
857 Representative immunoblot of LDHA and LDHB in the indicated H9c2-derived cell lines. **(F)** Fold change
858 of intracellular palmitate in *Ldha*^{-/-}, *Ldhb*^{-/-}, or *Ldha*^{-/-};*Ldhb*^{-/-} H9c2 cell lines in response to treatment with
859 palmitate-conjugated BSA (Pal) relative to BSA vehicle control (BSA). **(G)** Changes in ¹³C enrichment of
860 extracellular lactate in *Ldha*^{-/-}, *Ldhb*^{-/-}, or *Ldha*^{-/-};*Ldhb*^{-/-} H9c2 cell lines in response to treatment with
861 palmitate-conjugated BSA. **(H)** Concentration of ¹³C-labelled extracellular lactate in *Ldha*^{-/-}, *Ldhb*^{-/-}, or
862 *Ldha*^{-/-};*Ldhb*^{-/-} H9c2 cell lines in response to BSA vehicle control (BSA) or palmitate-conjugated BSA (Pal)
863 treatment. **(I)** Changes in intracellular ¹³C enrichment of pyruvate in *Ldha*^{-/-}, *Ldhb*^{-/-}, or *Ldha*^{-/-};*Ldhb*^{-/-}
864 H9c2 cell lines in response to treatment with palmitate-conjugated BSA. **(J)** Concentration of intracellular
865 ¹³C-labelled pyruvate in *Ldha*^{-/-}, *Ldhb*^{-/-}, or *Ldha*^{-/-};*Ldhb*^{-/-} H9c2 cell lines in response to BSA vehicle
866 control (BSA) or palmitate-conjugated BSA (Pal) treatment. **(F – G)** All experiments were performed in
867 triplicate. Data are presented as mean \pm SD. *p < 0.05, **p < 0.01, ***p < 0.001, ****p < 0.0001,
868 determined by one-way ANOVA and Sidak's multiple comparison test.

869

870 **Figure S4. Tissues expression of lactate dehydrogenase segragate in an isoform-specific manner.**

871 Differential gene expression of LDHA and LDHB across human tissues. (A) Scatter plot depicting median
872 transcripts per million (TPM) for LDHA and LDHB. Note logarithmic axes. (B) Heatmap depicting median
873 TPM for LDHA and LDHB across human tissues. Data obtained through GTEx Portal.

874 **Table S1. Phosphoserine-ENO2 data collection and refinement statistics.**

Wavelength (Å)	1.00000
Resolution range (Å)	39.89 - 2.10 (2.175 - 2.10)*
Space group	P 2 ₁ 2 ₁ 2 ₁
Unit cell (Å)	68.0498 108.38 117.929
(°)	90, 90, 90
Total reflections	2203993 (188723)*
Unique reflections	50504 (4644)*
Multiplicity	43.6 (38.5)*
Completeness (%)	96.58 (90.06)*
Mean I/sigma(I)	20.52 (1.92)*
Wilson B-factor(Å ²)	25.70
R-merge	0.9095 (3.46)*
R-meas	0.92 (3.508)*
R-pim	0.1353 (0.5575)*
CC1/2	0.931 (0.539)*
CC*	0.982 (0.837)*
Reflections used in refinement	49880 (4573)*
Reflections used for R-free	2482 (226)*
R-work	0.1802 (0.2715)*
R-free	0.2348 (0.3264)*
CC(work)	0.849 (0.706)*
CC(free)	0.841 (0.649)*
Number of non-hydrogen atoms	7008
macromolecules	6666
ligands	44
solvent	298
Protein residues	870
RMS(bonds)(Å)	0.007
RMS(angles)(°)	0.88
Ramachandran favored (%)	96.88
Ramachandran allowed (%)	2.89
Ramachandran outliers (%)	0.23
Rotamer outliers (%)	1.85
Clashscore	4.72
Average B-factor(Å ²)	30.34
macromolecules	30.16
ligands	43.30
solvent	32.47

875 *Statistics for the highest-resolution shell are shown in parentheses.

876 **Table S2. AP-3-fumarase data collection and refinement statistics.**

Wavelength (Å)	1.323630
Resolution range (Å)	49.80 - 2.15 (2.20 - 2.15)*
Space group	P 6 ₅ 2 2
Unit cell (Å)	190.90, 116.24, 190.90
(°)	90, 120, 90
Total reflections	2660677 (178767)*
Unique reflections	67921 (4478)*
Multiplicity	39.2 (39.9)*
Completeness (%)	100 (100)*
Mean I/sigma(I)	15.0 (1.1)*
Wilson B-factor	43.3
R-merge	0.25 (4.82)*
R-meas	0.26 (4.95)*
R-pim	0.056 (1.088)*
CC1/2	0.999 (0.458)*
CC*	-
Reflections used in refinement	67877
Reflections used for R-free	3399
R-work	0.1858(0.3100)*
R-free	0.2088(0.3300)*
CC(work)	0.965(0.6406)*
CC(free)	0.955(0.6746)*
Number of non-hydrogen atoms	7191
macromolecules	6847
ligands	44
solvent	300
Protein residues	922
RMS deviations (bonds)	0.0031
RMS deviations (angles)	1.266
Ramachandran favored (%)	96.82
Ramachandran allowed (%)	3.18
Ramachandran outliers (%)	0.00
Rotamer outliers (%)	0.84
Clashscore	2.92
Average B-factor	52.00
macromolecules	52.09
ligands	56.03
solvent	50.97

877 *Statistics for the highest-resolution shell are shown in parentheses.

878

879 **Other Supplementary Materials for this manuscript include the following:**

880 **Data S1. MIDAS metabolite library**

881 **Data S2. FIA-MS properties of MIDAS metabolites**

882 **Data S3. MIDAS proteins**

883 **Data S4. MIDAS protein-metabolite interactions**